Contrib Mineral Petrol (2001) 141: 322–346
DOI 10.1007/s004100000233

**Leander Franz · Rolf L. Romer · Reiner Klemd
Robert Schmid · Roland Oberhänsli · Thomas Wagner
Dong Shuwen**

Eclogite-facies quartz veins within metabasites of the Dabie Shan (eastern China): pressure–temperature–time–deformation path, composition of the fluid phase and fluid flow during exhumation of high-pressure rocks

Received: 17 May 2000 / Accepted: 22 November 2000 / Published online: 31 March 2001

Abstract Metabasites in the high-pressure unit of the southern Dabie Shan (eastern China) contain quartz veins with high-pressure mineral assemblages. Two veins with the parageneses quartz–paragonite–ankerite–rutile and quartz–kyanite–talc–zoisite–rutile–calcite (pseudomorph after aragonite) as well as quartz–kyanite–paragonite–garnet–omphacite were investigated in detail. Host rocks of these veins are garnet amphibolites with eclogitic relics and quartz eclogites, respectively. The oldest phase of deformation (D1) is recorded in the eclogite, which displays a schistosity with shape alignment of high-pressure minerals such as omphacite, phengite and garnet. An estimate of the metamorphic P–T conditions yields 19–21 kbar at 570–620 °C for the eclogites. Fluid inclusion studies reveal a primary, low-salinity aqueous fluid phase responsible for the formation of the quartz veins. This is in correspondence with calculations of phase equilibrium curves on minerals of the vein paragenesis, which yield P–T conditions of 19.4 kbar and 591 °C in the presence of an aqueous fluid phase. Geochronology using the U–Pb system of rutile gives evidence for a Triassic minimum age of 207–221 Ma for the vein formation, which fits in the geotectonic framework of the orogen. This rather wide age range arises from the heterogeneous nature of the initial lead isotopic composition, reflecting the heterogeneous sources of the lead and the fluid phase. Part of the fluid was probably generated by prograde dehydration reactions in the country rocks of the veins, whereas strong evidence is also given for the derivation from an older basement, which also underwent subduction. The veins may have formed by extensive hydraulic fracturing or by volume reduction during eclogitisation of the crust. Subsequent to the formation of the veins, great parts of the high-pressure rocks experienced an intensive, syn-tectonic (D2) amphibolite facies metamorphism at 8.5–10.5 kbar and 590–645 °C, indicating isothermal decompression during exhumation. In the course of this exhumation, pseudosecondary CO_2 inclusions were trapped in quartz of the veins. The last recorded stage of the retrograde overprint took place under static, greenschist facies conditions (450–480 °C) in the stability field of kyanite. The shape of the metamorphic P–T path for this stage is reflected by the fluid phase, which either re-equilibrated during this event or penetrated the rock on fractures. These findings show that fluid flow during subduction-related high-pressure metamorphism and subsequent uplift is rather complex; the fluid phase may originate from different sources and may interact with country rocks in the form of a chromatographic column transforming mineral assemblages, and also changing its own character.

L. Franz (✉)
Institut für Mineralogie, TU Bergakademie Freiberg,
Brennhausgasse 14, 09596 Freiberg, Germany
E-mail: lfranz@mineral.tu-freiberg

R.L. Romer
GeoForschungsZentrum Potsdam, Telegrafenberg,
14473 Potsdam, Germany

R. Klemd · T. Wagner
Institut für Mineralogie, Am Hubland,
Universität Würzburg, 97070 Würzburg, Germany

R. Schmid · R. Oberhänsli
Institut für Geowissenschaften, Universität Potsdam,
Karl-Liebknechtstraße 24, 14455 Potsdam, Germany

D. Shuwen
Institute of Geomechanics, Chinese Academy of Geological
Science, 100081 Beijing, China

Editorial responsibility: J. Hoefs

Introduction

Quartz veins, which are a common feature in metamorphic rocks, are generally interpreted to form syn-metamorphically because of high fluid pressure, giving rise to extension (e.g. Yardley 1986). This high fluid pressure often results from dehydration reactions during prograde metamorphism, which may induce hydraulic fracturing

in the rock (Voll 1960; Yardley 1983). These fractures enhance and channelise the fluid flow in the rock and allow the precipitation of quartz as well as the formation of other metamorphic minerals that also occur in the host rock (Etheridge 1983). Mineral assemblages of such veins are usually/often generated during prograde greenschist facies conditions and may incorporate quartz, albite, calcite and, in some cases, sheet silicates such as chlorite and biotite (Voll 1969). In other cases, however, mineral assemblages in such veins indicate formation during peak pressure and temperature conditions (e.g. Austrheim 1987, 1990; Manning 1994; Ague 1997; Becker et al. 1999; Brunsmann et al. 2000), whereas in some instances quartz veins may also form near the end of a metamorphic loop (e.g. von Raumer 1984). As these veins always have a very specific relation concerning their textures and mineral assemblages to the metamorphic host rock, they may serve as a tool to unravel the tectonometamorphic evolution as well as the character of the fluid phase and its flow during metamorphism.

This paper presents a combination of petrological, geochronological, and fluid inclusion studies on high-pressure veins and their host rocks to constrain the metamorphic path as well as the composition and specific properties of the syn-metamorphic fluid phase (i.e. the P–T–t–d–*x* conditions) in quartz eclogites from the Dabie Shan (eastern China). We demonstrate that the fluid phase in Dabie Shan high-pressure rocks seems to be rather uniform in composition as early trapped aqueous fluid inclusion in quartz and omphacite in quartz eclogite of the Taihu area observed by You et al. (1996) show great affinities to our findings. The mineral assemblage used to derive the P–T conditions of vein formation includes up to 5-cm large rutile crystals. Geochronology of this rutile, therefore provides constraints on the generation of the mineral assemblage of these veins. Dating of this rutile, furthermore, is attractive as rutile has grown during vein formation and is not inherited or derived from the wallrock. Although it is debated whether rutile U–Pb ages represent cooling or formation ages (e.g. Mezger et al. 1989; Santos Zalduegui et al. 1996) the U–Pb age of rutile will constrain the exhumation history and its initial lead isotopic composition provides a fingerprint to the fluid source.

Geological setting and position of the veins

The Dabie Shan forms part of the Qinling collisional belt between the Yangtze and Sino-Korean cratons in east-central China (Mattauer et al. 1985). Continental northward subduction and subsequent exhumation of the Yangtze plate led to a complex, tectonically imbricated sequence of deformed metamorphic rocks. From south to north it can be subdivided into the Yangtze-foreland fold-and-thrust belt, the blueschist, the high-pressure amphibolite, the high-pressure (HP) quartz-bearing eclogites, the ultrahigh-pressure (UHP) coesite-bearing eclogites, and the 'northern orthogneiss' units, as well as the Luzhenguan and Foziling 'groups' in the greenschist facies (e.g. Okay 1993; Hacker et al. 1996, 2000; Liou et al. 1996). The peak P–T conditions for the highest grade rocks during the Palaeozoic/Mesozoic orogeny have recently been constrained at 40–48 kbar and <750 °C (Schmid et al. 2000).

Presently available chronological studies on the HP and UHP rocks report ages of 800–700 Ma for the protoliths and 240–220 Ma for the HP to UHP event (Ames et al. 1993, 1996; Li et al. 1993; Xiao et al. 1995; Rowley et al. 1997; Hacker et al. 1998). Initial uplift to crustal levels (e.g. Hacker et al. 2000) was followed by Cretaceous to Cenozoic extensional processes, facilitating exhumation to the surface and intrusions of syenitic to tonalitic plutons at ~140 Ma ago (Ratschbacher et al. 2000).

The area south of Lake Hualiangting (Fig. 1) is situated in the HP terrain of Dabie Shan and is largely dominated by white mica- and garnet-bearing orthogneisses, metasediments and lenses of quartz eclogites and garnet amphibolites. Large quartz-dominated veins are associated with eclogites and garnet amphibolites, which show eclogitic relics. The oldest recognisable deformation event (D1) occurred under eclogite facies conditions and led to a shape alignment of high-pressure minerals in the eclogites and the formation of the S1 schistosity, which follows in general a NW–SE trend with a south-westward dip of 30–40°. Subsequent to D1, the formation of the quartz veins occurred on fractures oblique to S1. The D2 deformation took place under amphibolite facies conditions creating the S2-foliation in the amphibolites and gneisses. The orientation of the S2-foliation is parallel–subparallel to the S1-schistosity in the eclogites.

Two occurrences of quartz veins were investigated. The first vein [see HPV1 (high-pressure quartz vein) in Fig. 1] is located within ankerite-bearing garnet amphibolites and outcrops near the road on the slope south of Lake Hualiangting [GPS location: N 30 28,1361 E 116 08,3745; source of samples HPV1 (qtz-vein, rutile crystal) and 98117 (wallrock garnet amphibolite)]. It has a thickness of ~1 m and formed on a steep, NE–SW striking fracture that lies discordantly to the SW-dipping S2-foliation of the amphibolites. The vein consists mainly of quartz, randomly oriented white mica flakes, and large ankerite crystals as well as rutile (see Fig. 2a).

The second outcrop (see HPV2 in Fig. 1) is located to the east of the first locality near a road junction [GPS location: N30 27,6919 E 116 09,5657; source of samples HPV2a,b,c (qtz-veins), HPV2b (rutile crystal) and 98118 (host-eclogite)]. There, several interconnected quartz veins occur within fresh eclogites. The eclogitic host rocks of the vein often show a compositional layering with alternating quartz-rich and garnet–omphacite-rich sections and in part reveal a penetrative foliation with aligned omphacite prisms. Part of the eclogite, however, has a compact, porphyroblastic texture. The size of the quartz veins strongly varies from <1 to >50 cm. The distribution and orientation of mineral phases in these veins are highly variable. Two representative sections

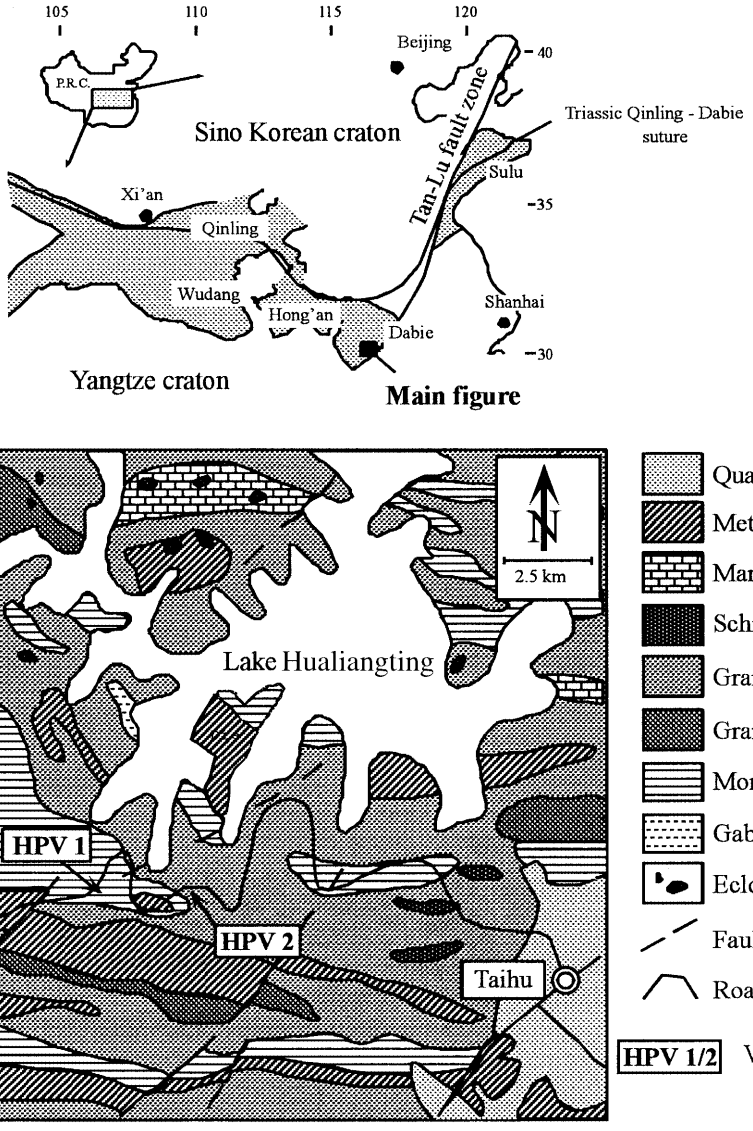

Fig. 1 Geographic position of the Dabie Shan and geological sketch map with the sample locations. Map modified after You et al. (1996) and the geological map of Dabie mountains area of Anhui province from Anhui Institute of Regional Geological Survey (AIRGS, 1997)

within this network of veins were investigated. The first vein (HPV2a) has a thickness of ~10 cm and mainly consists of quartz with up to 5-cm-long rutile prisms and minor amounts of kyanite and talc. The second vein (HPV2b; HPV2c) has an irregular, gnarly shape (see Fig. 2b). Beside quartz, it is made up of kyanite, talc, paragonite, pseudomorphs of calcite after aragonite, large zoisite prisms, rutile, as well as garnet and omphacite. Both investigated veins strike ENE–WSW and are steeply dipping towards NNW. They discordantly cut the S1-foliation in the eclogites, which is rather variable in this location showing a south-westward to south-eastward dip of 40–65°.

Petrography and mineral chemistry of veins and host rocks

Minerals described below were analysed using a JEOL JXA-8900R electron microprobe at the University of Freiberg or with Cameca SX-50 and SX-100 electron microprobes at the GFZ Potsdam. Major and minor elements were determined at 15 kV acceleration voltage and a beam current of 20 nA with counting times of 20 s for Si, Al, Mg, Ca, Sr, Ba and K, and 30 s for Fe, Ni, Na, Cr, Mn and Ti. The standard sets of the Smithsonian Institute (Jarosewich et al. 1980) and of CAMECA were used for reference. Selected microprobe analyses of the most important minerals are listed in Tables 1, 2, 3 and 4. The entire data set is available from the first author on request.

Quartz veins

The quartz veins in the two locations show similar textural features as they all formed on fractures that crosscut the main metamorphic foliation of their host rocks. The vein HPV1 shows a porphyroblastic texture in its centre with granoblastic quartz grains, randomly oriented white mica flakes, and large ankerite porphyroblasts. Occasionally, zoisite prisms appear. According to microprobe analyses, white mica is paragonite with a prominent amount of celadonite and minor amounts of muscovite ($Pg_{75-88}Cel_{11-16}Ms_{0-5}Mrg_{0-2}$). Ankerite yields an elevated amount of magnesite component and shows a chemical composition of $Cc_{53}Mgs_{34}Sid_{12}Rhc_{<1}$, which is very similar to the carbonate in the hosting garnet amphibolite (see below). At the immediate contact to the surrounding metabasites, dynamic recrystallisation led to the

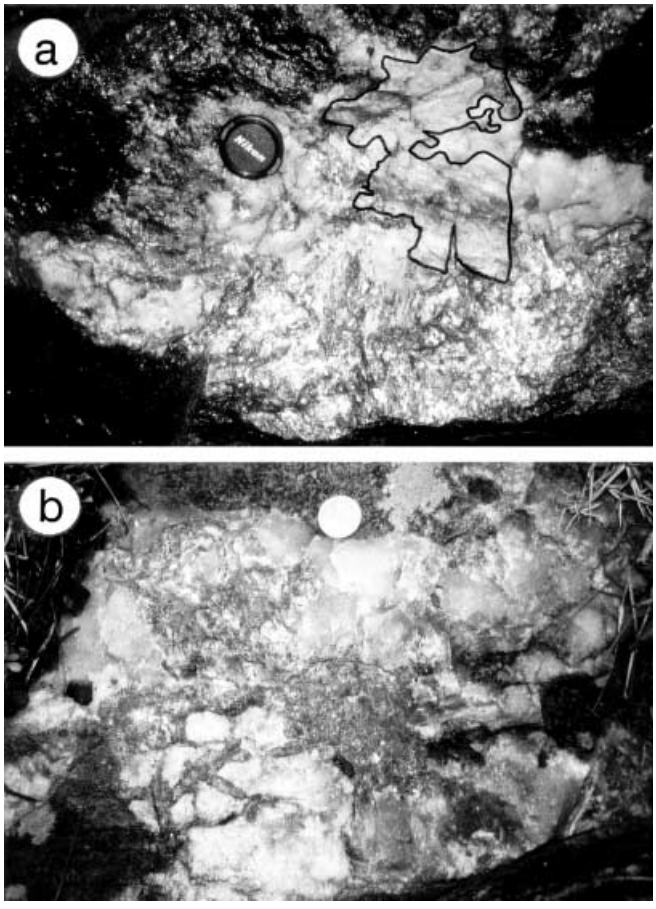

Fig. 2 **a** Photograph of vein HPV1 showing a large ankerite crystal (accentuated by an *ink line*) in a matrix of quartz and paragonite. **b** Photograph of vein HPV2b displaying randomly oriented zoisite prisms in the centre of the vein, short prismatic rutile (right of the zoisite) as well as kyanite and talc near the contact to the host eclogite. The diameter of the coin is 2.5 cm

formation of small quartz subgrains and new grains. This recrystallisation probably resulted from mylonitisation because of rheological contrasts between metabasite and quartz vein during the exhumation. To a smaller extent, similar dynamic recrystallisation features of vein quartz are found in intergranular positions. In the recrystallised sections near to the contact of the host rock, fragments of strongly chloritised garnet are observed, which reveal a weak chemical zoning with decreasing grossular contents ($Grs_{20–14}$) and increasing almandine and pyrope contents ($Alm_{58–62}$; $Pyp_{20–23}$) from core to rim. In some locations, a small retrograde rim with distinctly decreasing X_{Mg} [$=Mg/(Mg+Fe)$] values and increasing grossular contents ($Alm_{57}Pyp_{18}Grs_{23}Sps_2$) is developed. Around garnet, numerous small flakes of biotite had formed and were later affected by a strong chloritisation. As the composition of these garnet fragments strongly resembles the garnet in the host rock, they are anticipated to be xenocrysts from the wallrock.

The samples from vein HPV2 in the second location also show granoblastic quartz grains and randomly oriented porphyroblasts in their central parts. Near the contact to the host eclogite, however, kyanite, zoisite and talc tend to grow perpendicular to the vein walls, which is especially prominent in sample HPV2b and HPV2c. This texture may be interpreted as stretched crystals in the sense of Ramsay and Huber (1983) or as fibrous veins (Passchier and Trouw 1996) and thus probably developed during the progressive opening of the fracture. Remarkably, there is no dynamic recrystallisation of vein quartz near the contact of the eclogite. The modal mineral amount of these veins is rather variable. Sample HPV2a, for example, is dominated by quartz and large rutile prisms, whereas kyanite and talc are accessory phases. In thicker parts of the quartz vein, rather complex associations of minerals are found. Specimen HPV2b contains the mineral assemblage quartz–kyanite–zoisite–talc ± calcium carbonate (former aragonite as indicated by the crystal shape) ± rutile. This section of the vein also bears fragments of garnet xenocrysts, whose composition is rather uniform ($Alm_{49–51}Pyp_{31–34}Grs_{14–16}Sps_2$) and strongly resembles the rim composition of the eclogitic garnet. Other parts of the vein are dominated by quartz–paragonite ($Pg_{90–94}Mrg_{2–3}Ms_{3–6}$)–kyanite. Eventually, small symplectitc intergrowths of diopside-rich clinopyroxene and albite occur. Especially paragonite and zoisite are often surrounded by small, secondary rims of albite ($An_{0.6–6.4}$) and tremolite. In specimen HPV2c, garnet from the host rock displays a preferential growth into the vein, which is evident by its elongated rim section (cf. Fig. 3). The inner part of this garnet reveals a compositional zoning with increasing Mg contents at the expense of Ca (core: $Alm_{54}Pyp_{18}Grs_{26}Sps_1$; near rim: $Alm_{54}Pyp_{28}Grs_{18}Sps_1$), which is quite similar to the garnet of the host eclogite (cf. Fig. 4 and Table 4). The newly grown rim section is characterised by distinctly higher Mg contents and lower almandine and grossular components ($Alm_{46–49}Pyp_{30–35}Grs_{15–19}Sps_1$). Garnet is accompanied by paragonite ($Pg_{91–94}Mrg_{0–1}Ms_{5–8}$), kyanite, and omphacite ($Jd_{36–40}$), which experienced a strong decomposition to magnesio-hornblende. Like garnet, all these minerals show a growth perpendicular to the wall of the vein. Representative mineral analyses from the vein assemblages are listed in Tables 1, 2, 3 and 4.

Host rocks

The host rocks of the veins mainly consist of metabasites, namely garnet amphibolites in case of HPV1 and eclogites in location HPV2.

Garnet amphibolites with a remarkable variability in texture are the host of vein HPV1. The amphibolites usually show a penetrative S2-foliation, which is made up of aligned hornblende, plagioclase, chlorite, and in part elongated garnet. Accessories are epidote, biotite, ilmenite and rutile. Two distinctly different generations of garnet can be distinguished in sample 98117-3: garnet porphyroblasts (see pGrt in Table 4) with diameters of up to 1 cm often show an elongation perpendicular to the main foliation and reveal irregular compositional zoning patterns. The likely prograde growth of these crystals, however, is indicated by the highest X_{Mg} values near the rims although retrograde sections may be developed where an intergrowth with hornblende appears. Small elongated garnet grains with a length of 0.5–1.3 mm are also aligned in the foliation and reveal a homogeneous composition in the core ($Alm_{60–62}Pyp_{15–17}Grs_{19–21}Sps_{2–3}$; see aGrt in Table 4), which corresponds to the rim sections of the large garnet porphyroblasts with maximum X_{Mg}. The rim sections of these small garnet grains also give evidence for a retrograde overprint with a composition of $Alm_{65}Pyp_{13}Grs_{17}Sps_5$. The occurrence of these different types of garnet is interpreted in the following way: porphyroblastic, irregularly zoned types highlight a polyphase evolution with prograde growth and subsequent fracturing and rearrangement of small pieces, stripped from the formerly broken crystals, by ductile flow. Although the prograde growth may have taken place prior or during eclogite facies conditions, the rupturing and recrystallisation may have been the consequence of exhumation and amphibolite facies overprint. The fact that growth zoning was not erased in spite of the structural and metamorphic overprint of the garnet is probably because of its relatively large size compared with garnet from other amphibolites (cf. Fig. 4). Small, elongated garnet crystals may have formed as a result of syn-tectonic amphibolite facies crystallisation. According to the scheme of Leake et al. (1997), Ca-amphibole prisms aligned in the S2-foliation can mainly be classified as tschermakite and magnesio-hornblende, whereas small xenoblastic grains intergrown with the rim section of garnet are pargasite (see Table 3). The aligned prisms show a slight increase in Al and Ti towards the rim, whereas the small grains are unzoned. Following the scheme of Hey (1954), chlorite of sample

Table 1 Selected microprobe analyses of white mica, biotite, talc, and kyanite of the investigated rocks

wt%	HPVI[a] Vein Pg	HPVI Vein Pg	HPV2a Vein Pg	HPV2a Vein Pg	BPV2c Vein Pg	BPV2c Vein Pg	HPV2a Vein Tlc	HPV2a Vein Tlc	HPV2a Vein Tlc	98117-4 GA Pg	98117-4 GA Pg	98117-3 GA Bt	98117-3 GA Bt	198118-2 QE Ph	98118-2 QE Ph	98118-5 QE Pg	98118-5 QE Pg
SiO_2	49.72	48.70	46.58	46.71	46.56	46.31	61.92	61.25	61.09	46.97	46.38	36.33	36.86	52.77	52.06	47.09	47.21
TiO_2	0.06	0.03	0.07	0.06	0.07	0.02	0.01	0.01	0.00	0.09	0.12	2.24	2.11	0.14	0.22	0.11	0.16
Al_2O_3	35.72	37.61	39.47	39.60	3941	39.18	0.30	0.14	0.20	4013	39.86	17.29	16.75	24.56	24.89	39.45	39.54
Cr_2O_3	0.00	0.00	0.02	0.02	0.00	0.02	0.00	0.00	0.01	0.04	0.00	0.04	0.04	0.00	0.00	0.03	0.03
MgO	0.64	0.11	0.12	0.13	0.15	0.23	29.58	29.06	29.07	0.19	0.17	11.73	11.88	4.76	4.53	0.18	0.15
CaO	0.19	0.13	0.28	0.30	0.04	0.14	0.02	0.01	0.01	0.31	0.31	0.06	0.00	0.01	0.00	0.46	0.36
MnO	0.00	0.01	0.01	0.00	0.00	0.03	0.01	0.00	0.00	0.00	0.00	0.07	0.06	0.05	0.05	0.00	0.01
FeO	0.51	0.40	0.66	0.68	0.73	0.64	3.00	3.44	3.04	0.57	0.67	17.48	17.49	1.14	1.15	0.56	0.56
BaO	0.06	0.05	0.12	0.11	0.10	0.00	0.00	0.05	0.00	0.00	0.00	0.34	0.35	0.00	0.00	0.02	0.07
Na_2O	5.63	7.18	7.42	7.15	7.01	7.41	0.07	0.05	0.07	6.89	6.72	0.20	0.13	0.44	0.63	7.70	7.42
K_2O	2.78	0.85	0.57	0.61	0.65	0.98	0.02	0.00	0.01	0.75	0.91	9.86	10.05	10.83	10.49	0.27	0.58
Total	**95.32**	**95.07**	**95.32**	**95.36**	**94.73**	**95.16**	**94.94**	**94.00**	**93.49**	**95.93**	**95.14**	**95.64**	**95.72**	**94.70**	**94.02**	**95.86**	**96.08**
Cations (O = 11)																	
Si	3.188	1112	2∼984	2.988	2995	2.976	3.981	3.986	3.988	2.981	2.972	2.747	2.784	3.527	3.503	2.994	2.998
Ti	0.003	0.002	0.003	0.003	0.003	0.001	0.000	0.000	0.000	0.004	0.006	0.127	0.120	0.007	0.011	0.005	0.007
Al	2.700	2.833	2.980	2.985	2.987	2.983	0.023	0∼011	0.015	3.002	3.011	1.541	1.491	1.934	1.973	2.956	2.958
Cr	0.000	0.000	0.001	0.001	0.000	0.001	0.000	0.000	0.000	0.002	0.000	0.002	0.002	0.000	0.000	0.001	0.001
Mg	0.061	0.010	0.012	0.012	0.014	0.022	2.835	2.819	2.829	0.018	0.016	1.322	1.338	0.474	0.454	0.017	0.014
Ca	0.013	0.009	0.019	0.020	0.003	0.010	0.002	0.000	0.000	0.021	0.022	0.005	0.000	0.006	0.000	0.032	0.024
Mn	0.000	0.000	0.000	0.000	0.000	0.002	0.001	0.000	0.000	0.000	0.000	0.004	0.004	0.003	0.003	0.000	0.001
Fe	0.028	0.022	0.035	0.036	0.039	0.034	0.162	0.187	0.166	0.030	0.036	1.105	1.105	0.064	0.065	0.030	0.030
Ba	0.002	0.001	0.003	0.003	0.003	0.000	0.000	0.001	0.000	0.000	0.000	0.010	0.010	0.000	0.000	0.000	0.002
Na	0.700	0.890	0.921	0.887	0.874	0.923	0.009	0.006	0.009	0.847	0.836	0.029	0.019	0.057	0.082	0.949	0.913
K	0.227	0.069	0.047	0.050	0.053	0.080	0.002	0.000	0.000	0.061	0.074	0.951	0.969	0.923	0.901	0.022	0.047
Total	**6.922**	**6.949**	**7.006**	**6.985**	**6.972**	**7.033**	**7.013**	**7.011**	**7.009**	**6.967**	**6.972**	**7.844**	**7.843**	**6.989**	**6.991**	**7.007**	**6.995**

[a] HPV, High-pressure quartz vein; GA, garnet amphibolite; QE, quartz eclogite; ph, phengite; other mineral abbreviations according to Kretz (1983)

Table 2 Selected microprobe analyses of zoisite, clinozoisite, chlorite and carbonate minerals

wt%	HPV1[a] Zo	HPV1 Vein Zo	HPV2a Vein Zo	HPV2a Vein Zo	98117-4 GA Czo	98117-4 GA Czo	98118-2 QE Zo	98118-5 QE Zo	wt%	98117-3 GA Chl	98117-3 GA Chl	wt%	HPV1 Vein Ank	HPV1 Vein Ank	HPV2a Vein Cc/Arg	HPV2a Vein Cc/Arg	98117-3 GA Ank
SiO_2	38.29	37.55	37.86	38.31	37.71	38.09	38.14	38.64	SiO_2	25.37	25.39	SiO_2	0.10	0.00	0.06	0.03	0.00
TiO_2	0.12	0.14	0.07	0.09	0.10	0.11	0.09	0.14	TiO_2	0.10	0.10	TiO_2	0.00	0.00	0.01	0.02	0.00
Al_2O_3	25.55	25.47	27.95	27.93	28.18	29.11	29.38	29.24	Al_2O_3	21.61	21.82	Al_2O_3	0.00	0.00	0.00	0.00	0.00
Cr_2O_3	0.03	0.01	0.00	0.00	0.02	0.00	0.04	0.00	Cr_2O_3	0.00	0.00	Cr_2O_3	0.00	0.00	0.00	0.00	0.00
Fe_2O_3	11.30	11.32	6.44	6.75	6.48	5.91	5.58	5.95	Fe_2O_3	0.49	0.21	MgO	13.87	14.10	0.10	0.16	14.43
MgO	0.07	0.06	0.23	0.13	0.20	0.13	0.33	0.23	MgO	17.59	17.56	CaO	30.21	30.11	55.63	55.73	29.78
CaO	23.54	23.57	23.41	23.82	23.34	23.54	23.35	23.77	CaO	0.10	0.04	MnO	0.62	0.70	0.04	0.07	0.56
MnO	0.05	0.08	0.05	0.04	0.04	0.04	0.06	0.03	MnO	0.10	0.11	FeO	9.45	9.60	0.05	0.10	9.75
BaO	0.01	0.00	0.00	0.00	0.01	0.00	0.00	0.00	FeO	21.98	22.04	BaO	0.00	0.00	0.00	0.00	0.02
Na_2O	0.02	0.00	0.02	0.00	0.00	0.01	0.03	0.01	Na_2O	0.02	0.00	Na_2O	0.00	0.00	0.00	0.08	0.00
K_2O	0.00	0.00	0.00	0.02	0.01	0.01	0.01	0.00	K_2O	0.00	0.00	CO_2	45.17	45.34	43.92	44.14	45.46
Total	**98.97**	**98.20**	**96.03**	**97.09**	**96.08**	**96.94**	**97.01**	**98.01**	**Total**	**87.36**	**87.27**	**Total**	**99.42**	**99.85**	**99.78**	**100.33**	**100.00**
Cations (0 = 25)									Cations (O = 28)			Cations (O = 3)					
Si	5.978	5.921	5.990	6.003	5.964	5.954	5.948	5.972	Si	5.291	5.289	Si	0.002	0.000	0.001	0.000	0.000
Ti	0.014	0.017	0.008	0.011	0.012	0.013	0.011	0.016	Ti	0.016	0.016	Ti	0.000	0.000	0.000	0.000	0.000
Al	4.000	4.000	5.000	5.000	5.000	5.000	5.000	5.000	Al	5.311	5.357	Al	OMO	0.000	0.000	0∼000	0000
Cr	0.004	6.001	.000	0.000	0.003	0.000	0.005	0.000	Cr	0.000	0.000	Cr	0.000	0.000	0.000	0.000	0.000
Fe^{3+}	1.327	1.344	0.767	0.796	0.771	0.695	0.655	0.692	Fe^{3+}	0.077	0.033	Mg	0.335	0.340	0.002	0.004	0.347
Mg	0.016	0.014	0.055	0.031	0.046	0.030	0.077	0.052	Mg	5.467	5.453	Ca	0.525	0.521	0.994	0.991	0.514
Ca	3.938	3.982	3.970	3.999	3.955	3.942	3.901	3.936	Ca	0.021	0.009	Mn	0.009	0.010	0.001	0.001	0.008
Mn	0.006	0.011	0.006	0.006	0.006	0.005	0.008	0.004	Mn	0.018	0.019	Fe^{2+}	0.128	0.130	0.001	0.001	0.131
Ba	0.000	0.000	0.000	0.000	0.001	0.000	0.000	0.000	Fe^{2+}	3.841	3.843	Ba	0.000	0.000	0.000	0.000	0.000
Na	0.007	0.001	0.005	0.001	0 .000	0.002	0.010	0.004	Na	0.009	0.000	Na	0.000	0.000	0.000	0.003	0.000
K	0.000	0.000	0.001	0.003	0.002	0.001	0.002	0.000	K	0.000	0.000	C	1.000	1.000	1.000	1.000	1.000
Total	**15.994**	**16.023**	**16.015**	**16.010**	**16.012**	**16.006**	**16.017**	**16.004**	**Total**	**20.043**	**20.016**	**Total**	**1.998**	**2.000**	**1.999**	**2.001**	**2.000**

[a] HPV, High-pressure quartz vein; GA, garnet amphibolite; QE, quartz eclogite; ph, phengite; other mineral abbreviations according to Kretz (1983)

Table 3 Selected microprobe analyses of clinoamphibole and plagioclase

wt%	HFV2a[a] Vein Cam	HPV2c Vein Cam	98117-3 GA Cam	98117-3 GA Cam	98117-4 GA Cam	98117-4 GA Cam	98118-2 QE Cam	98118-2 QE Cam	98118-5 QE Cam	98118-5 QE Cam	wt%	HPV2a Vein Pl	HPV2a Vein Pl	98117-3 GA Pl	98117-3 GA Pl	98117-4 GA Pl	98118-2 QE Pl	98118-5 QE Pl
SiO_2	56.89	50.63	42.27	42.34	48.95	40.81	38.52	49.74	53.22	42.96	SiO_2	66.59	68.01	63.79	61.95	63.58	64.92	64.75
TiO_2	0.01	0.07	0.56	0.49	0.43	0.17	0.02	0.03	0.06	0.03	$A1_2O_3$	20.32	18.92	21.80	23.67	21.83	19.49	22.74
Al_2O_3	0.95	6.67	13.95	14.27	7.94	14.79	19.05	8.98	10.68	16.04	MgO	0.00	0.01	0.00	0.01	0.48	1.56	0.06
Fe_2O_3	1.63	2.06	6.13	3.21	0.65	3.51	3.84	4.25	3.29	3.27	CaO	1.36	0.14	3.16	4.90	3.55	2.17	3.69
Cr_2O_3	0.00	0.02	0.00	0.00	0.00	0.01	0.00	0.00	0.05	0.01	MnO	0.00	0.01	0.00	0.00	0.01	0.03	0.02
MgO	22.15	16.06	8.90	8.79	12.00	8.90	9.45	12.07	14.98	10.66	FeO	0.04	0.15	6.24	0.04	0.67	1.49	0.40
CaO	12.08	10.53	9.58	10.63	11.79	11.56	10.63	15.67	6.50	9.78	BaO	0.00	0.00	0.01	0.00	0.01	0.00	0.00
MnO	0.04	0.11	0.12	0.16	0.12	0.11	0.11	0.11	0.12	0.21	Na_2O	11.01	11.71	10.06	9.03	9.66	9.88	9.82
FeO	2.39	7.66	13.50	14.90	14.12	14.88	11.56	3.82	5.20	11.41	K_2O	0.02	0.06	0.03	0.05	O∼05	0.01	0.04
Na_2O	0.90	2.15	1.90	1.96	1.27	2.61	3.47	3.50	4.25	3.81	**Total**	**99.35**	**99.00**	**99.08**	**99.65**	**99.85**	**99.44**	**101.51**
K_2O	0.05	0.15	0.53	0.89	0.09	0.21	0.08	0.04	0.08	0.18	Cations (O=8)							
Total	**97.07**	**96.13**	**97.44**	**97.64**	**97.36**	**97.55**	**96.73**	**98.21**	**98.44**	**98.34**	Si	2.939	3.003	2.843	2.756	2.922	2.887	2.821
Cations (O=23)											Al	1.057	0.985	1.145	1.241	1.142	1.023	1.168
Si	7.873	7.304	6.311	6.331	7.170	6.141	5.763	7.076	7.325	6.257	Mg	0.000	0.001	0.000	0.001	0.032	0.103	0.004
Ti	0.001	0.008	0.063	0.055	0.047	0.019	0.002	0.003	0.007	0.003	Ca	0.064	0.006	0.151	0.233	0.169	0.103	0.172
Al	0.155	1.135	2.455	2.514	1.370	2.622	3.359	1.506	1.732	2.753	Mn	0.000	0.001	0.000	0.000	0.000	0.001	0.001
Fe^{3+}	0.169	0.224	0.688	0.362	0.072	0.397	0.432	0.455	0.341	0.358	Fe	0.002	0.006	0.009	0.001	0.025	0.055	0.014
Cr	0.000	0.003	0.000	0.000	0.000	0.001	0.000	0.000	0.006	0.001	Ba	0.000	0.000	0.000	0.000	0.000	0.000	0.000
Mg	4.569	3.453	1.981	1.959	2.619	1.997	2.107	2.560	3.074	2.315	Na	0.942	1.002	0.869	0.779	0.831	0.853	0.829
Ca	1.791	1.628	1.532	1.702	1.850	1.864	1.704	2.388	0.959	1.526	K	0.001	0.004	0.002	0.003	0.003	0.001	0.002
Mn	0.005	0.013	0.015	0.020	0.014	0.015	0.014	0.013	0.014	0.025	**Total**	**5.004**	**5.007**	**5.020**	**5.014**	**5.024**	**5.028**	**5.011**
Fe^{2+}	0.276	0.924	1.685	1.864	1.730	1.873	1.447	0.455	0.599	1.389	End members:							
Na	0.241	0.601	0.550	0.569	0.360	0.762	1.005	0.964	1.134	1.077	An	6.4	0.6	14.7	23.0	16.8	10.8	17.2
K	0.008	0.028	0.101	0.169	0.017	0.039	0.016	0.007	0.014	0.034	Ab	93.5	99.0	85.1	76.7	82.9	89.1	82.6
Total	**15.088**	**15.322**	**15.380**	**15.545**	**15.250**	**15.730**	**15.849**	**15.426**	**15.203**	**15.739**	Or	0.1	0.4	0.2	0.3	0.3	0.1	0.2

[a] HPV, High-pressure quartz vein; GA, garnet amphibolite; QE, quartz eclogite; ph, phengite; other mineral abbreviations according to Kretz (1983)

Table 4 Selected microprobe analyses of garnet, omphacite and clinopyroxene from symplectites (sym) of the metabasites. *aGrt* Small, aligned garnet crystals of amphibolite sample 98117-3; *pGrt* large garnet porphyroblasts. Fe_2O_3 in garnet was added by iteration until the amount of Al needed to calculate the listed end members equalled the amount of Al^{VI} present; Fe_2O_3 in clinopyroxene was determined after the method of Droop (1987)

wt%	HPV1[a] Vein Grt core	HPV2c Vein Grt core	HPV2c Vein Grt rim	98117-3 GA aGrt core	98117-3 GA aGrt rim	98117-3 GA pGrt core	98117-4 GA Grt core	98117-4 GA Grt rim	98118-2 QE Grt core	98118-2 QE Grt rim	98118-5 QE Grt core	98118-5 E Grt rim
SiO_2	38.78	37.81	38.35	38.22	37.94	37.98	37.52	38.44	38.82	39.71	38.47	39.58
TiO_2	0.05	0.05	0.00	0.04	0.07	0.06	0.09	0.01	0.08	0.03	0.08	0.12
Al_2O_3	21.79	21.81	22.64	21.73	21.24	21.18	21.20	21.62	21.70	2186	20.93	21.75
Cr_2O_3	0.00	0.10	0.06	0.00	0.02	0.00	0.00	0.03	0.00	0.01	0.00	0.00
Fe_2O_3	0.00	0.18	0.00	0.00	0.00	0.00	0.49	0.00	0.00	0.00	0.89	0.59
MgO	5.77	6.11	9.14	3.74	2.68	3.11	2.42	4.80	4.17	9.73	4.13	9.64
CaO	5.02	8.78	6.47	6.56	8.53	7.39	9.75	6.58	11.98	4.67	11.13	5.44
MnO	0.73	0.43	0.43	0.68	2.23	0.64	4.27	0.76	1.47	0.62	0.42	0.59
FeO	28.21	23.24	21.51	30.32	28.19	30.78	24.07	27.95	21.35	22.75	23.52	22.18
Na_2O	0.03	0.01	0.03	0.00	0.04	0.04	0.02	0.01	0.03	0.02	0.00	0.00
Total	**100.38**	**98.52**	**98.63**	**101.29**	**100.93**	**101.19**	**99.83**	**100.21**	**99.59**	**100.39**	**99.57**	**99.89**
Cations (O = 12)												
Si	3.015	2.968	2.956	2.989	2.992	2.992	2.982	3.007	3.020	2.998	3.014	3.012
Ti	0.003	0.003	0.000	0.002	0.004	0.004	0.006	0.001	0.005	0.002	0.005	0.007
Al	1.996	2.018	2.057	2.003	1.974	1.966	1.985	1.994	1.999	2.034	1.933	1.950
Cr	0.000	0.006	0.004	0.000	0.001	0.000	0.000	0.002	0.000	0.000	0.000	0.000
Fe^{3+}	0.000	0.010	0.000	0.000	0.000	0.000	0.029	0.000	0.000	0.000	0.053	0.034
Mg	0.669	0.714	1.050	0.436	0.315	0.366	0.287	0.560	0.483	1.095	0.482	1.093
Ca	0.419	0.739	0.534	0.549	0.721	0.624	0.830	0.552	0.999	0.378	0.934	0.444
Mn	0.048	0.029	0.028	0.045	0.149	0.043	0.287	0.050	0.097	0.040	0.028	0.038
Fe^{2+}	1.834	1.526	1.386	1.983	1.859	2.028	1.600	1.829	1.389	1.437	1.541	1.411
Na	0.004	0.002	0.005	0.000	0.006	0.006	0.003	0.002	0.004	0.002	0.000	0.000
Total	**7.988**	**8.014**	**8.019**	**8.007**	**8.022**	**8.027**	**8.008**	**7.996**	**7.985**	**7.986**	**7.989**	**7.989**
End members:												
Uvar:	0.0	0.30	0.18	0.0	0.1	0.0	0.0	0.1	0.0	0.0	0.0	0.0
Grs + A-dr:	14.1	24.27	17.64	18.2	23.6	20.4	27.6	18.4	33.7	12.8	31.3	14.9
Alm:	61.8	50.73	46.23	65.8	61.1	66.3	53.3	61.1	46.8	48.7	51.6	47.2
Sps:	1.6	0.96	0.94	1.5	4.9	1.4	9.6	1.7	3.3	1.4	0.9	1.3
Prp:	22.5	23.76	35.01	14.5	10.3	11.9	9.5	18.7	16.3	37.1	16.1	36.6

wt%	HPV2c Vein Omp	98117-4 GA Cpx sym	98118-2 QF Omp	98118-2 QE Omp	98118-5 QE Omp	98118-5 QE Omp
SiO_2	55.76	54.86	56.20	55.89	54.98	54.68
TiO_2	0.03	0.02	0.03	0.01	0.11	0.13
$A1_2O_3$	9.67	8.32	12.05	11.99	8.74	870
Cr_2O_3	0.05	0.01	0.08	0.08	0.00	0.03
Fe_2O_3	0.55	0.00	1.57	2.19	1.13	1.88
MgO	11.13	9.73	7.86	7.80	17.33	17.56
CaO	13.89	16.67	11.41	11.29	7.67	7.65
MnO	0.01	0.10	0.05	0.00	0.03	0.02
FeO	3.72	6.95	2.85	2.47	5.99	5.51
Na_2O	5.45	4.16	7.70	7.76	4.12	4.05
K_2O	0.02	0.03	0.00	0.01	0.00	0.03
Total	**100.28**	**100.85**	**99.80**	**99.49**	**100.10**	**100.24**
Cations (O = 6)						
Si	1.977	1.974	1.990	1.986	1.941	1.929
Ti	0.001	0.001	0.001	0.000	0.003	0.003
Al	0.404	0.353	0.503	0.502	0.364	0362
Fe^{3+}	0.015	0.000	0.042	0.059	0.030	0.050
Cr	0.001	0.000	0.002	0.002	0.000	0.001
Mg	0.588	0.522	0.415	0.413	0.912	0.924
Ca	0.528	0.643	0.433	0.430	0.290	0.289
Mn	0.000	0.003	0.002	0.000	0.001	0.001
Fe^{2+}	0.110	0.209	0.084	0.073	0.177	0.163
Na	0.375	0.290	0.529	0.535	0.282	0.277
K	0.001	0.001	0.000	0.000	0.000	0.001
Total	**4.000**	**3.995**	**4.000**	**4.000**	**4.000**	**4.000**
End members after Banno (1959)						
Jd:	40.06	31.2	50.7	49.5	44.9	41.9
Acm:	1.53	0.0	4.3	6.0	44	7.2
Aug:	58.41	68.8	45.0	44.5	50.7	51.0

[a] HPV, High-pressure quartz vein; GA, garnet amphibolite; QE, quartz eclogite; ph, phengite; other mineral abbreviations according to Kretz (1983)

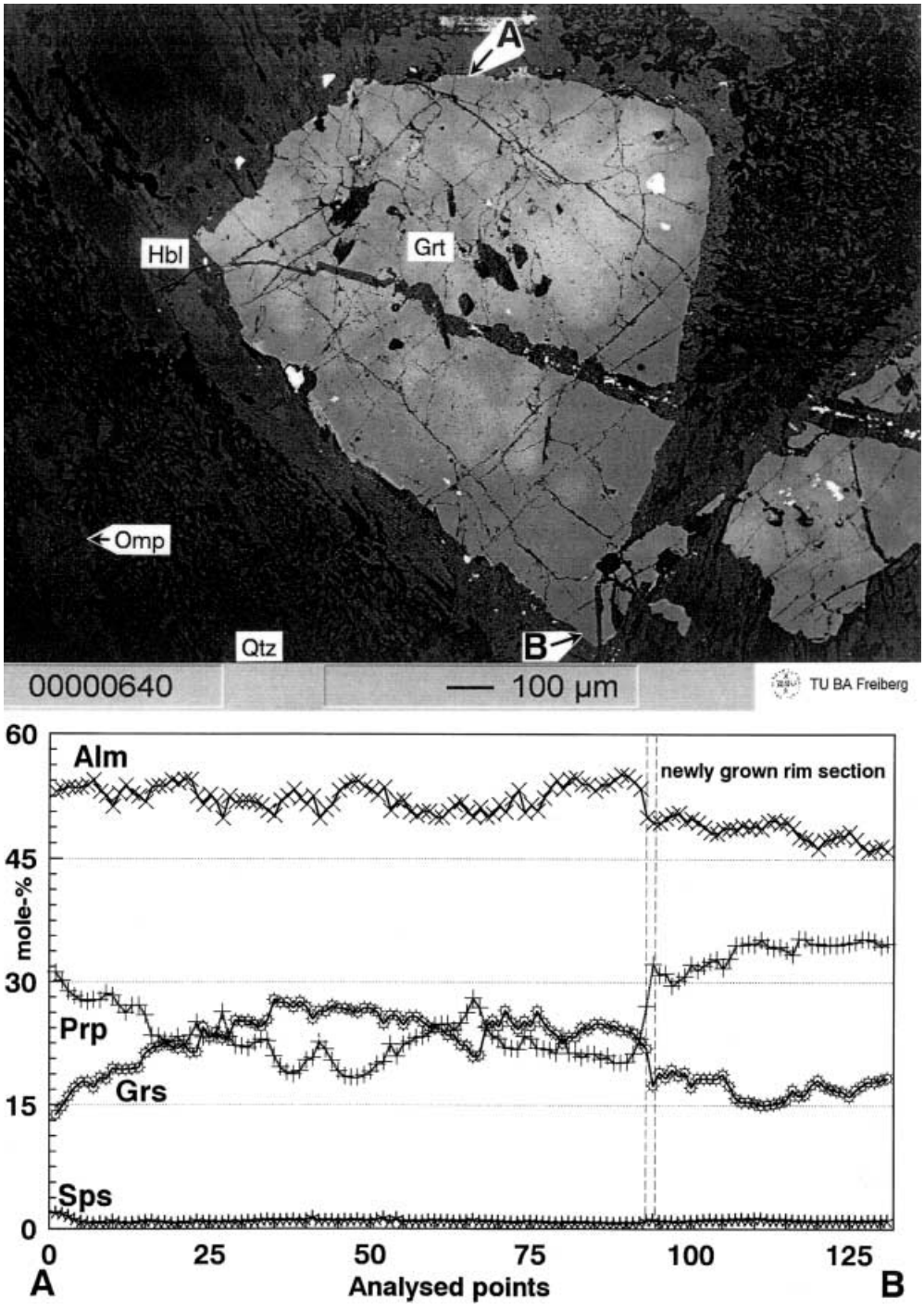

Fig. 3 Backscattered electron image of a garnet, which shows a preferential growth into the vein (i.e. towards point *B*) and microprobe profile through this garnet. Note the similarity of the compositional zoning in the core of this garnet to the garnet in the host eclogite (sample 98118-2 in Fig. 4)

98117-3 is ripidolite with X_{Fe} values of ~0.42. According to the method of Laird and Albee (1981), chlorite only contains minor amounts of ferric iron. Like chlorite, biotite also shows an alignment in the S2-foliation. Microprobe analyses reveal TiO_2 contents of ~2 wt% and X_{Mg} values of ~0.54. Selected analyses of biotite and chlorite are listed in Table 2. Plagioclase occurs as aligned crystals in the foliation, as euhedral intergrowth with hornblende at the garnet rims and as small rims around garnet. Aligned plagioclase shows relatively constant composition of about 14 mol% An, whereas plagioclase intergrown with hornblende has slightly elevated Ca contents of $An_{15–19}$, and the highest An contents (18–23 mol%) are recorded in plagioclase rimming garnet (see Table 3). Epidote is often intergrown with plagioclase and also shows an alignment in the foliation. The small prisms are virtually unzoned with X_{Ps} of ~0.22. Ilmenite forms small tablets in the matrix and charge balance constraints indicate elevated contents of ferric iron with up to 15 mol% of haematite component. Carbonate in the matrix is ankerite with $Cc_{50}Mgs_{35}Sid_{15}Rhc_{<1}$ and SrO + BaO contents of less than 0.03 wt% (Table 2).

Garnet amphibolite in the immediate vicinity of vein HPV1, i.e. in a layer of about 5 cm around the vein, shows a massive, por-

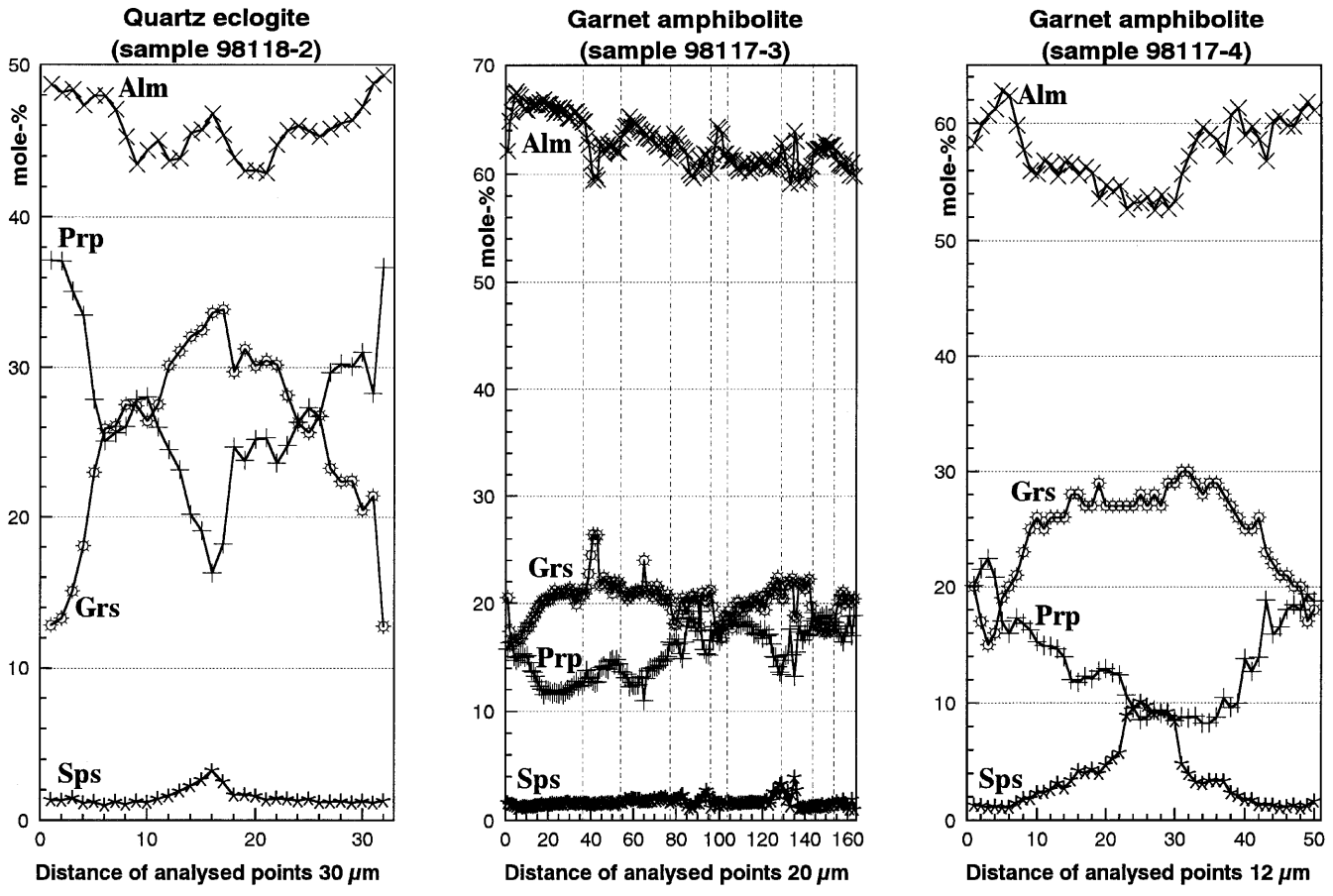

Fig. 4 Comparison of microprobe profiles through compositionally zoned garnet porphyroblasts from a quartz eclogite (sample 98118-2) and garnet amphibolite (sample 98117-4), and through an elongated garnet of garnet amphibolite sample 98117-3. *Thin lines* indicate zones of former rupturing and recrystallisation during amphibolite facies ductile shearing

phyroblastic texture. An example of this can be observed in sample 98117-4, where garnet crystals up to 1 cm in diameter are rimmed by green hornblende and plagioclase, and the matrix is made up of quartz, epidote, paragonite, ankerite and prismatic, fine grained symplectites. Accessories are rutile, ilmenite and rare apatite. Microprobe profiles through large garnet porphyroblasts of sample 98117-4 reveal compositional zonation patterns with strongly elevated spessartine and grossular contents in the centre and a composition of $Alm_{53–54}Pyp_{9–10}Grs_{26–27}Sps_{9–10}$. Towards the rim, an increase in X_{Mg} and a decrease in the spessartine and grossular component is observed and only in the outermost rim section is this pattern reversed, which reflects the prograde growth followed by a retrograde overprint (cf. Fig. 4). Garnet composition near the rim is $Alm_{61–62}Pyp_{18–19}Grs_{18–19}Sps_{1–2}$ (cf. Table 4) and this composition is also found in small garnet grains that are totally surrounded by symplectites of clinopyroxene, hornblende and plagioclase and probably completely re-equilibrated during the peak of the amphibolite-facies overprint. Two distinctly different generations of Ca-amphibole are observed. Amphibole forming small rims around garnet as well as millimetre-sized prisms in the matrix is pargasite and ferropargasite according to the scheme of Leake et al. (1997). The crystals yield X_{Fe} values of 0.45–0.57 (midpoint Fe^{3+} calculation using the method of Papike et al. 1974) and show a certain variability in Si, Al, and Ti contents although a common zonation pattern is not observed. Small grains within the symplectites are magnesio-hornblende with distinctly lower X_{Fe} values than the rest of the hornblende population. They are intergrown with fine plagioclase lamellae yielding anorthite contents of 15–19 mol% (for microprobe analyses of plagioclase and Ca-amphibole see Table 3). In the centre of the symplectites (sym), clinopyroxene with variable jadeite content of 7–32 mol% and X_{Fe} values of 0.21–0.28 are present (see Cpx symp in Table 4). They are armoured by plagioclase and sometimes rimmed by hornblende and probably represent the first stage of omphacite and garnet breakdown following the peak of eclogite facies metamorphism. Epidote forms large prisms in the matrix but also fine grains in the symplectites with both types showing a very similar composition, i.e. X_{Ps} values of 0.12–0.15. Paragonite, which is often strongly decomposed, yields a composition of $Pg_{88–91}Cel_{0–2}Ms_{6–8}Mrg_{2–4}$, thus resembling the paragonite on the adjacent quartz vein (see Table 1). Similar to sample 98117-3, ilmenite yields an elevated amount of ferric iron which results in a haematite component of up to 10 mol%.

Eclogites hosting vein HPV2 show porphyroblastic textures with euhedral garnet in a matrix of omphacite, zoisite and white mica. Alignment of zoisite and omphacite often defines a foliation/lineation, whereas randomly scattered garnet porphyroblasts occur both as atoll-types enclosing white mica, rutile, and omphacite, and as inclusion-free grains. A retrograde development of pale-green hornblende mainly took place at the rim of the garnet, whereas clinopyroxene–plagioclase symplectites developed around omphacite. Two representative eclogite samples (98118-2 and 98118-5), which were investigated with the microprobe, show slightly different mineral assemblages. Sample 98118-2 yields the paragenesis omphacite–zoisite–garnet–phengite ± rutile, whereas sample 98118-5 displays the same assemblage except for the white mica, which is paragonite. Both samples reveal prominent compositional zoning in garnet with increasing almandine ($Alm_{43–52}$) and pyrope ($Prp_{18–38}$) contents from core to rim at the expense of grossular ($Grs_{34–13}$) and spessartine ($Sps_{4–1}$). This type of zonation pattern is mainly present in large, inclusion-free garnet crystals (cf. Fig. 4 and Table 4), whereas it is less pronounced or even completely missing

in atoll-type garnet. Steadily increasing X_{Mg} values from core to rim highlight the prograde development of this kind of garnet, whereas retrograde rims with slightly decreasing X_{Mg} are only recorded in sections with secondary amphibole overgrowth. Omphacite in both samples shows jadeite contents of 48–54 mol% (sample 98118-2) and 42–45 mol% (sample 98118-5), respectively. While there was no zoning in jadeite content, an increase in X_{Mg} from core to rim could be observed in most omphacite grains. Charge balance constraints following Droop (1987) point to ferric iron contents of 0–40% of total iron in the omphacite, which is variable from grain to grain (cf. Table 4). This variability may result from (1) uncertainties in charge balance because of low Fe_{total} contents and (2) a retrograde overprint leading to partial decomposition of the omphacites (i.e. alteration to hornblende). Zoisite hardly reveals any zoning except for a little higher amount of ferrous iron in the core section of some specimen. Phengite grains of sample 98118-2 yield Si contents of 3.4–3.5 p.f.u. with relatively constant X_{Mg} values of 0.86–0.88, whereas paragonite of sample 98118-5 has a composition of $Prg_{93-95}Ms_{2-5}Mrg_{2-3}$ (cf. Table 1). Secondary pyroxene in the symplectites is diopside with minor amounts of jadeite (Jd_{11-30}; see Table 4), which shows intergrowth with plagioclase of An_{9-13} (sample 98118-2) and An_{17-25} (sample 98118-5). Secondary amphibole displays a rather variable composition, which may differ distinctly within the same section. In the symplectites of sample 98118-2, pargasite and edenite are observed. Sample 98118-5 bears pargasite, edenite, tschermakite and magnesio-hornblende near garnet rims and within symplectites, whereas large, blue-green intergranular grains are barroisite (amphibole classification of Leake et al. 1997). Most of these minerals show Fe^{3+} contents of 20–30% using the midpoint calculation method of Papike et al. (1974). Microprobe analyses of amphibole and plagioclase are listed in Table 3.

Pressure–temperature evolution

Eclogite

As evident from clinozoisite aggregates pseudomorphous after porphyroblastic lawsonite, as well as from inclusions of glaucophane in garnet of eclogites south of lake Hualiangting (Castelli et al. 1998), a clockwise prograde P–T path can be inferred for these rock. This is also indicated by typical prograde compositional zonation patterns in garnet of the investigated eclogites (cf. Fig. 4), which points to maximum temperatures of less than 650–700 °C (Yardley 1977; Schliestedt 1980; Spear 1991). Furthermore, chemical zoning in garnet and omphacite testifies to equilibrium conditions between these minerals in their rim sections. Garnet–clinopyroxene thermometry performed on garnet and nearby omphacite (not in direct contact with the garnet) yields temperatures of 570–620 °C at 22 kbar for sample 98118-2 using the latest calibration of Krogh (2000). The use of this calibration gave results very similar to other calibrations performed on HP rocks (e.g. Krogh 1988; Brey and Köhler 1990), whereas older calibrations (e.g. Ellis and Green 1979) overestimated these temperatures by 70–90 °C. Application of garnet–phengite thermometry (Green and Hellman 1988) on garnet rims and core sections of phengite results in temperatures of 635–711 °C, but because of the missing estimate for ferric iron in phengite, these temperatures have to be regarded as maximum values. Minimum pressures can be constrained for the eclogites using the jadeite content of omphacite (Holland 1980, 1990), which points to 15–16 kbar at a temperature of 600 °C. Similar minimum-pressures are obtained with phengite barometry using the approach of Massonne (1991). Barometry of the inverse tschermaks exchange among garnet, clinopyroxene and phengite of Waters and Martin (1993; updated calibration of 1996 with activity models of Newton and Haselton (1981) and Holland (1990) for garnet and omphacite, respectively) results in pressures of 19–21 kbar at temperatures of 600 °C for garnet rim sections with the highest X_{Mg} values, adjacent jadeite rims and phengite cores with the highest Si contents (i.e. 3.50–3.53 p.f.u.). An estimate of the P–T-conditions during exhumation is hampered by evident mineral chemical disequilibria within the eclogites as already indicated by the mainly coronitic textures. Temperature calculations for the Fe–Mg-exchange between garnet rims and symplectitic hornblende using the calibration of Graham and Powell (1986) result in a wide scatter of 460–750 °C. Similarly, secondary clinopyroxene in the symplectites show strongly variable temperatures of 370–650 °C for the Fe–Mg-exchange with the garnet rim using the Grt–Cpx thermometry of Krogh (2000).

Quartz veins

Because of a lack of critical mineral assemblages, an estimate of the P–T conditions during the formation of the quartz vein HPV1 is not possible. The lack of textural constraints furthermore precludes any ultimate statement about the time of its formation, although the presence of minerals such as paragonite and ankerite, which are also present in the adjacent relic eclogite, point to its generation under HP conditions.

Mineral textures and assemblages in quartz veins HPV2 offer the opportunity to directly constrain the P–T conditions during formation. The growth of garnet next to omphacite, paragonite and kyanite in sample HPV2c highlights the generation of this vein under eclogite facies conditions. Minimum pressures of 12.5–13.5 kbar are estimated by the jadeite barometry of Holland (1980; 1990), whereas the Grt–Cpx-geothermometer of Krogh (2000) points to temperatures of 580–630 °C. Maximum pressures for the formation of the veins are constrained by the reaction paragonite $\leftrightarrow$ kyanite + jadeite + H_2O. A calculation of the reaction curve using the TWEEQ-program of Berman (1991) and minerals of sample HPV2c yields pressures of 20–21.5 kbar at temperatures of 580–630 °C and a water activity of 1.0 (cf. Fig. 6). A reduction of the water activity would lead to a distinct decrease in pressure. For sample HPV2b, the P–T-X condition were modelled in the CaCMASH system with the TWEEQ-program of Berman (1991). The vein assemblage quartz–zoisite–kyanite–talc–aragonite as well as eclogitic garnet and the fluid phases H_2O and CO_2 (for which proof was given by fluid inclusion studies, see below) were selected for this

calculation. Values for H, V and S of aragonite given in the VERTEX program-package of Connolly (1990) were implemented into the TWEEQ database. A calculation of phase equilibrium curves including 17 mineral reactions (with three independent reactions) revealed an intersection at 19.6 kbar and 591 °C at a water activity of 0.88 and a CO_2 activity of 0.12 (Fig. 5). Although the two data sets used are not internally consistent, the incorporation of the aragonite data did not only lead to meaningful results concerning the thermobarometry, but also fitted well with the fluid inclusion studies (see below) thus justifying this extension of the database.

Garnet amphibolite

Syn-tectonic amphibolite facies metamorphism generated the D2 foliation, which can be well observed in the host rocks of vein HPV1. There, the strongly foliated garnet amphibolite sample 98117-3 reveals peak metamorphic temperatures of 590–630 °C, based on garnet rim sections and hornblende (midpoint Fe^{3+} estimate) using the calibration of Graham and Powell (1986). These temperatures are also obtained by garnet–chlorite thermometry (Dickenson and Hewitt 1986; Ghent et al. 1987). The garnet–hornblende–plagioclase–quartz geobarometer of Kohn and Spear (1990) indicates pressures of 9–10.5 kbar, which coincides with results of former calibrations for this assemblage (e.g. Kohn and Spear 1989). Similarly, pressures of 9.5–11 kbar were calculated using the GRIPS-geobarometer of Bohlen and Liotta (1986).

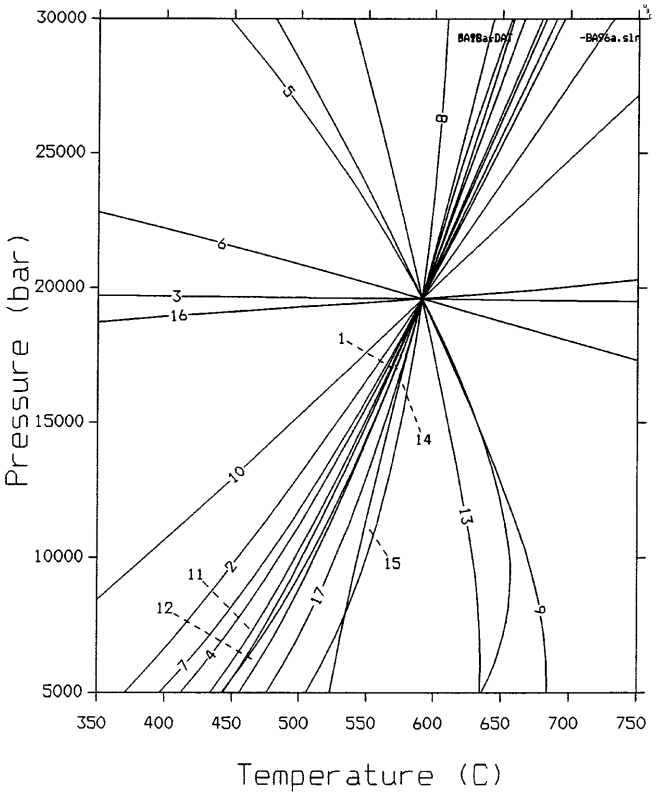

Fig. 5 Calculation of phase equilibrium curves in the CaCMASH system for the HP mineral assemblage of vein HPV2b using the TWEEQ program of Berman (1991). The calculation yields an intersection at 19.6 kbar and 591 °C at a water activity of 0.88 and a CO_2 activity of 0.12. Mineral reactions, activity models and thermodynamic data set see Appendix

Garnet amphibolite sample 97117-4 only locally reproduces these thermobarometric estimates. P–T-conditions of 8.5–10 kbar at 578–648 °C are calculated for garnet rims and adjacent plagioclase–hornblende–symplectites. Wider hornblende rims around garnet, however, yield unrealistically high temperatures of up to 750 °C for the Fe–Mg-exchange with the garnet, which may be caused by local mineral disequilibria. Clinopyroxene–plagioclase symplectites around garnet rims highlight an earlier metamorphic stage with elevated pressures. The symplectitic clinopyroxene shows jadeite contents of up to 32 mol%, which points to pressures of up to 13.5 kbar using the jadeite barometry of Holland (1980, 1990). These crystals also developed an Fe–Mg-exchange equilibrium with the garnet rims as indicated by temperatures of 560–615 °C calculated with the Grt–Cpx-thermometer of Krogh (2000).

Figure 6 shows the tectonometamorphic evolution in the southern Dabie Shan starting with a subduction-type prograde P–T path of the eclogites deduced from the observations of Castelli et al. (1998) and from compositionally zoned garnet. Peak metamorphic conditions can be estimated at 570–620 °C and 19–21 kbar, which is in accordance with earlier investigations and the absence of coesite (Okay 1993; Carswell et al. 1997). The error of this P–T-box would be ±2.5 kbar for the garnet–omphacite–phengite geobarometer of Waters and Martin (1993) and ±30 °C for the garnet–clinopyroxene geothermometer of Krogh (2000). In the light of our new and other published P–T estimates (e.g. Carswell et al. 1997), high temperatures (≥700 °C) for the quartz eclogites of southern Dabie Shan, as reported by Castelli et al. (1998) have to be considered as an over-estimate. HP-metamorphism was taking place syn-tectonically as evident from the penetrative D1 foliation with an alignment of high-pressure minerals such as omphacite, phengite and clinozoisite.

The formation of the quartz veins initiated at eclogite facies P–T conditions and was connected with the presence of H_2O-rich fluid phase. Their generation may be a consequence of extensive hydraulic fracturing caused by prograde metamorphic dehydration or of particular deformation episodes as a result of the bulk volume reduction during eclogitisation of the crust (e.g. Austrheim 1998). Fracturing and vein formation, however, may also have been triggered by extensional tectonic processes and fluid activity during the initial stages of exhumation.

In the course of the exhumation, symplectites of clinopyroxene and plagioclase developed in the eclogites and, subsequently, symplectites and coarse grained intergrowths of plagioclase and hornblende were gener-

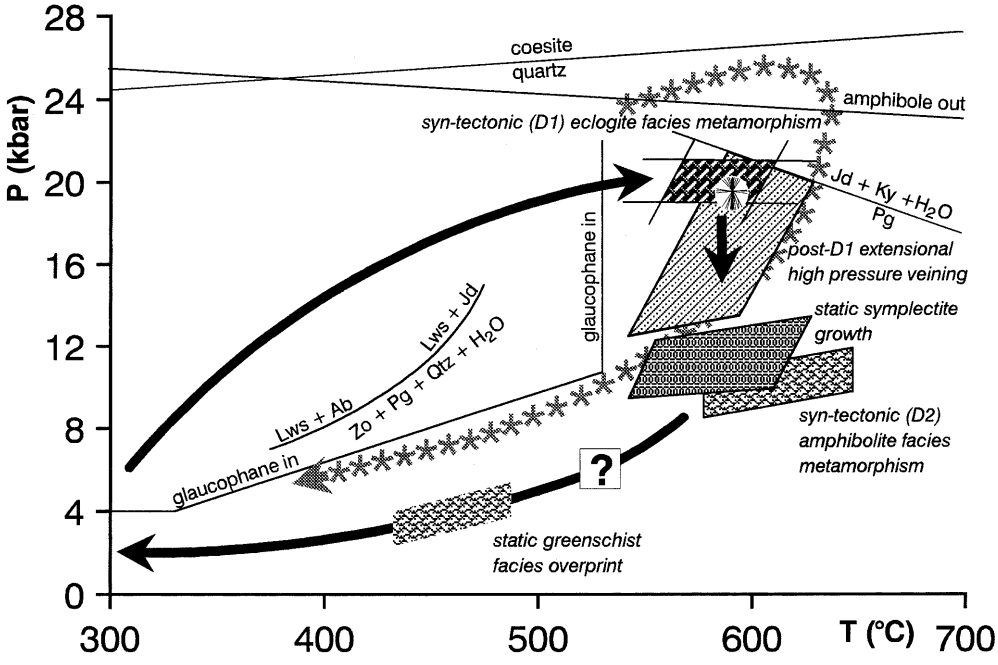

Fig. 6 P–T–t–d evolution of the HP-rocks from the Taihu region showing a prograde clockwise P–T evolution and an isothermal decompression. TWEEQ calculation for the post-D1 extensional veining the are indicated by intersecting phase equilibrium curves. Amphibole out reaction after Carswell (1990), glaucophane out after Maresch (1977), lawsonite out after Heinrich and Althaus (1981, 1988) and coesite quartz transformation as well as paragonite out reaction calculated with the TWEEQ program of Berman (1991; see Appendix). For comparison, the P–T path of Okay (1993) for quartz eclogites of the southern Dabie Shan is outlined by *grey stars*

ated. Later on, the penetrative D2 deformation affected the rock leading to the decomposition of the HP-assemblages as observed in the metabasic host rocks of vein HPV1, where schistose garnet amphibolite formed. Memory of the HP event was only preserved near the quartz vein, where symplectitic plagioclase and clinopyroxene were protected from the amphibolite facies overprint. There, the massive quartz vein may have acted as a chemical barrier hampering the penetration of fluid phase during the amphibolite facies overprint and thus preserving texture and mineral relics of the eclogite facies in its immediate vicinity. A mechanical shielding of the wallrock by the quartz vein can easily be excluded as the vein quartz should flow/deform much easier at temperatures of ~600 °C than its side wall. Formation of garnet amphibolite with the paragenesis hornblende–plagioclase–garnet–quartz took place at pressures of 8.5–10.5 kbar and temperatures of 590–645 °C.

At a very late stage, a static greenschist facies overprint led to the growth of albite and tremolite in the veins, for which temperatures of 450–480 °C may be estimated using Ti in Hbl thermometry of Colomby (1988) and Plg–Hbl geothermometry (e.g. Spear 1980). Although the exact retrograde path from the amphibolite facies stage cannot be reconstructed, it is rather probable that it remained within the stability field of kyanite as indicated by the sole occurrence of this alumino-silicate phase in the veins and the host rocks.

These data clearly highlight an isothermal decompression path for the eclogites in the Taihu area, which fits well in the pattern of P–T paths recorded for the Dabie Shan so far (e.g. Wang et al. 1990, 1992, 1995; Okay 1993; Liou et al. 1995, 1996; Carswell et al. 1997; cf. Fig. 6).

Fluid inclusion studies

Microthermometric measurements were performed using the USGS gas flow heating–freezing stage at the University of Würzburg. The estimated precision of final melting temperatures (Tm) and homogenisation temperatures of CO_2 inclusions is $\sim\pm 0.2$ °C; homogenisation temperatures of aqueous inclusions (Th) have a reproducibility of about ± 3 °C. A detailed description of the analytical and calibration procedures is given in Klemd et al. (1992). Calculation of densities and isochores was carried out using the FLINCOR program package (Brown 1989). Densities of H_2O–NaCl inclusions were calculated applying the equation of state of Zhang and Frantz (1987), whereas the equation of Holloway (1981) was used for CO_2 inclusions.

A total number of 161 fluid inclusions were microthermometrically investigated in four doubly polished thick sections of the high-pressure quartz vein samples HPV1, HPV2a and HPV2b. Fluid inclusions were found in kyanite and vein quartz. Based on textural criteria and fluid composition, three principal types of fluid inclusions can be distinguished:

Type 1. Texturally primary two-phase H_2O inclusions in kyanite (HPV2b). These inclusions are elongated and commonly display negative crystal morphologies (Fig. 7a). They occur either as individual inclusions or as groups oriented parallel to the *c*-axis of the kyanite crystals. The size of the inclusions is in the range of 10–150 μm; degrees of fill range usually between 80–90 vol%. This type of fluid inclusion represents the oldest recognisable generation of fluid inclusions.

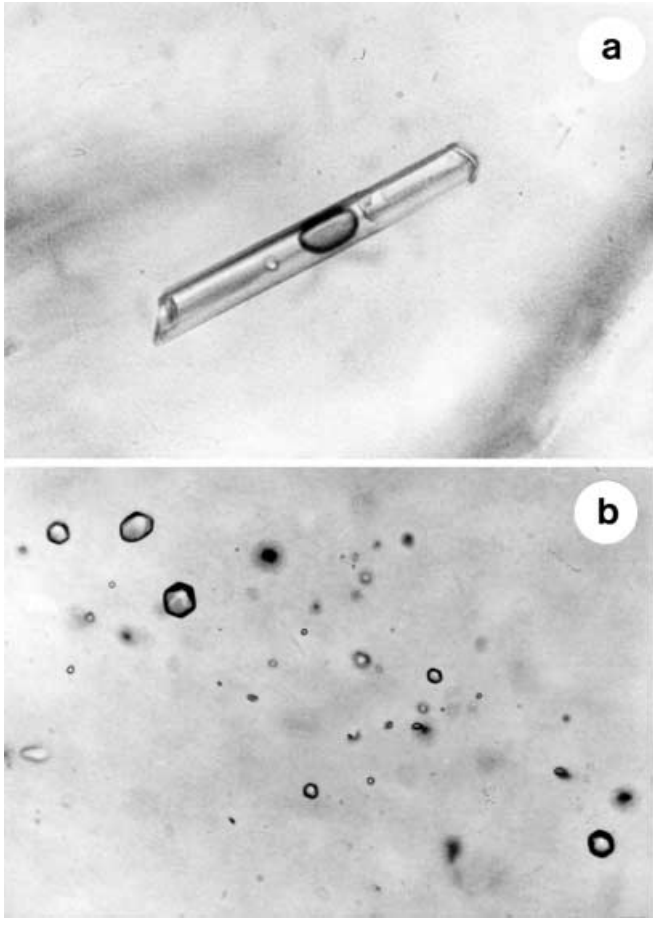

Fig. 7 Photomicrographs showing representative textures of fluid inclusions from the studied high-pressure veins, Dabie Shan. **a** Elongated primary two-phase H_2O inclusion (type 1) in kyanite; sample HPV2b. Width of field, 90 μm. **b** Trail of pseudosecondary monophase CO_2 inclusions (type 2) within recrystallised quartz; sample HPV2b. Width of field, 110 μm

Type 2. Texturally pseudosecondary monophase CO_2 inclusions in recrystallised vein quartz (HPV2b). Fluid inclusions of this type occur as clusters or trails that do not crosscut the grain boundaries between individual quartz grains. They display spheroidal/ellipsoidal or negative crystal shapes and are usually isometric (Fig. 7b). Inclusion sizes are in the range of 5–20 μm. This fluid inclusion type was trapped subsequent to type (1), because recrystallisation of quartz within the HP veins took place after crystallisation of kyanite.

Type 3. Secondary two-phase H_2O inclusions in recrystallised vein quartz (HPV1, HPV2a, HPV2b). This fluid inclusion type is very abundant in all investigated samples. In contrast to inclusions of type (2), they occur along healed microfractures crosscutting the recrystallisation texture of the vein quartz. They display very irregular shapes and high degrees of fill (>97 vol%). The size of inclusions is in the range of 10–35 μm.

Microthermometric results

Temperatures of final melting of primary aqueous two-phase inclusions in kyanite (type 1) are in the range between –0.4 and –1.2 °C (Table 5), corresponding to very low salinities of 0.7–2.1 wt% NaCl-equivalent (Fig. 8a). Eutectic melting was optically difficult to observe and occurred between –25 and –28 °C, indicating the presence of NaCl and KCl in the aqueous phase (Crawford 1981; Roedder 1984). Clathrate melting could not be observed. All aqueous fluid inclusions in kyanite homogenised into the liquid phase. Homogenisation temperatures range between 230 and 290 °C (Fig. 9) with a maximum at 260 ± 20 °C. The resulting densities are in the range of 0.71–0.83 g/cm^3. The salinities of these inclusions are rather constant as well as the homogenisation temperatures, therefore, it can be inferred that these inclusions were derived from a single homogeneous fluid phase. You et al. (1996) also exclusively observed type 1 inclusions with similar densities and textural occurrence in quartz and omphacite in coesite-free eclogites from the Taihu area.

The pseudosecondary CO_2 inclusions in recrystallised vein quartz (type 2) display final melting temperatures very close to –56.6 °C (–56.6 to –56.9), indicating the presence of insignificant amounts of N_2 or CH_4 only. Raman analysis only revealed CO_2. Consequently, neither temperatures of initial melting of the CO_2 phase nor additional phase transitions at low temperatures could be observed. The homogenisation temperatures of the CO_2 inclusions display a relatively wide variation ranging between –12.6 and 9.5 °C with no clear maximum detectable (Fig. 10). Homogenisation always took place

Table 5 Microthermometric results of fluid inclusions from the studied high-pressure veins

Sample and type of fluid inclusion	System	Tm CO_2 (°C)	Th CO_2 (°C)	Tm ice (°C)	Th tot (°C)	Density (g/cm^3)
HPV1						
Type 3, secondary in Qtz ($n=21$)	H_2O–NaCl–KCl			–0.5 to –2.0	158 to 200	0.973–0.932
HPV2a						
Type 3, secondary in Qtz ($n=27$)	H_2O–NaCl–KCl			–0.5 to –6.1	123 to 165	0.923–0.983
HPV2b						
Type 1, primary in Ky ($n=45$)	H_2O–NaCl–KCl			–0.4 to –1.2	233 to 293	0.713–0.827
Type 2, pseudosecondary in Qtz ($n=58$)	CO_2	–56.6 to –56.9	–12.6 to 9.5			0.924–0.997
Type 3, secondary in Qtz ($n=10$)	H_2O–NaCl–KCl			–0.4 to –0.6	150 to 173	0.904–0.928

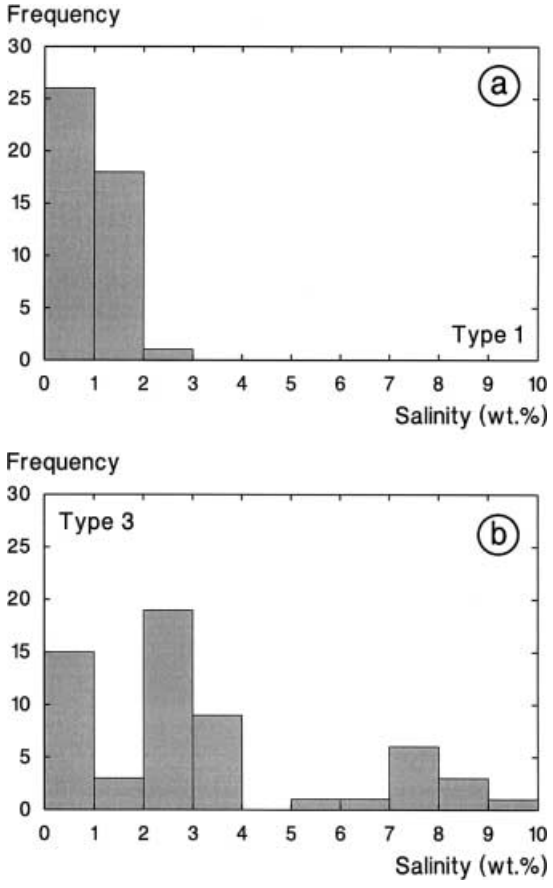

Fig. 8 Histograms displaying the salinities of two-phase H_2O inclusions (types 1 and 3). **a** Primary inclusions in kyanite (type 1); **b** secondary inclusions in quartz (type 3)

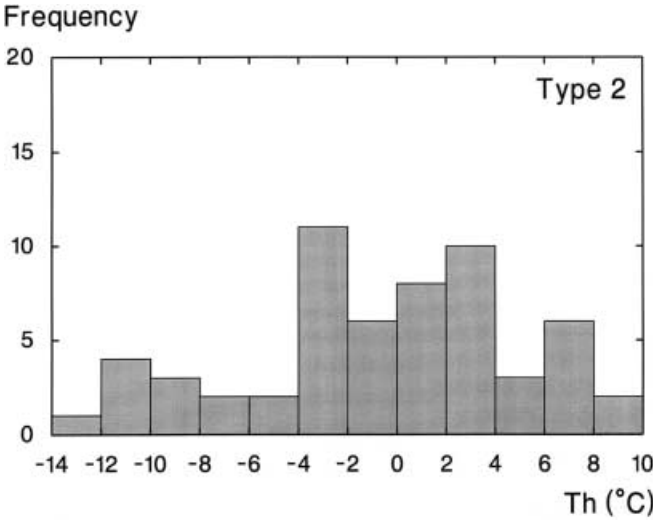

Fig. 9 Final melting (*Tm*) and homogenisation temperatures (*Th*) of both primary and secondary two-phase H_2O inclusions (types 1 and 3)

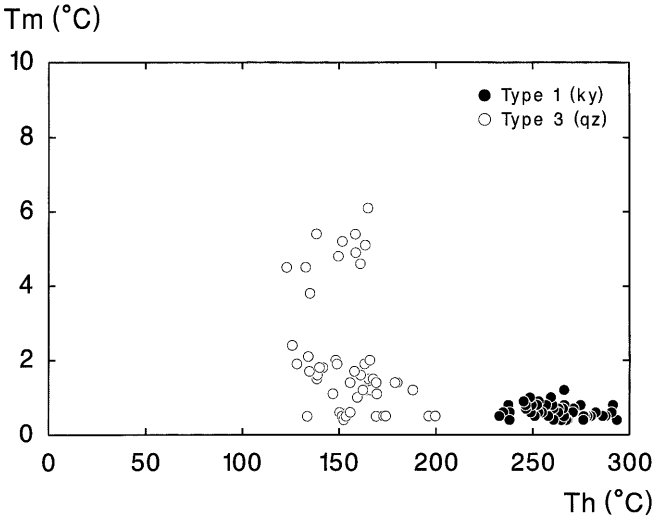

Fig. 10 Histogram of homogenisation temperatures of pseudosecondary CO_2 inclusions in vein quartz (type 2)

into the liquid phase and the calculated densities are in the range of 0.82–0.99 g/cm^3. No correlation between inclusion size and density (Th) can be observed (Fig. 11), although re-equilibrated fluid inclusion assemblages may display such a relationship as a result of pressure differences between internal pressure and confining pressure (Bodnar et al. 1989; Hall et al. 1991).

Secondary aqueous two-phase inclusions in vein quartz (type 3) display final melting temperatures in the range between –0.5 and –6.1 °C, corresponding to relatively low salinities of 0.7–9.3 wt% NaCl equivalent (Fig. 8b). Most inclusions of this textural type have salinities in the range of 0.7–4.0 wt% NaCl, including all inclusions from samples HPV2a and HPV1, whereas only 12 inclusions from sample HPV2b display somewhat higher salinities in the range 5.4–9.3 wt% NaCl equivalent. The resulting distribution is, therefore, distinctly bimodal (Fig. 8b and Fig. 9). Temperatures of eutectic melting are, although not generally observable, in the range between –17 and –29 °C, indicating the presence of NaCl and KCl. The absence of clathrate melting precludes the presence of significant amounts of CO_2. Homogenisation temperatures (homogenisation into the liquid phase) are in the range between 120 and 200 °C with a maximum at 160 ± 20 °C, resulting in densities of 0.87–0.98 g/cm^3. There is no correlation between final melting temperatures and homogenisation temperatures detectable (Fig. 9).

Conditions of trapping and sources of the fluids

Maximum and minimum density isochores were constructed for the respective highest- and lowest-density inclusions of each principal fluid inclusion type defined above. The isochores of both the low-salinity H_2O inclusions in kyanite (type 1) and the CO_2 inclusions in recrystallised quartz (type 2) overlap with the inferred retrograde P–T path during greenschist facies conditions in a relatively late exhumation stage of orogenic evolution (cf. Fig. 12). The calculated densities for these two

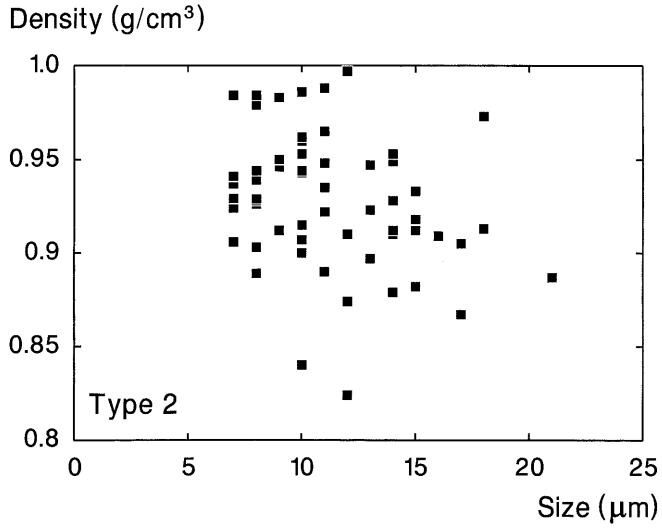

Fig. 11 Relationship between size and density of CO_2 inclusions (type 2) in vein quartz

inclusion types are too low to relate them to either the static symplectite growth or the subsequent syn-tectonic (D2) amphibolite facies metamorphism. However, it should be emphasised that back-reactions between the inclusion fluid and the kyanite host may have occurred. Back-reactions between inclusion fluids and mineral hosts other than quartz are a common process (Heinrich and Gottschalk 1995). A possible retrograde reaction such as kyanite + H_2O ± diaspore + quartz would have caused a density change in the low-salinity fluid. Salinities of the inclusion fluid would have been increased through such a back reaction. Solid inclusions along the inclusion walls have not been found by Raman analysis or petrographic means. The nature of very fine-grained (<1 μm) solids can only be identified by SEM methods (Heinrich and Gottschalk 1995). Based on the textural relationships of the H_2O inclusions in kyanite (type 1), which clearly reveal primary features, initial trapping of this inclusion type can be related to the post D1 stage of extensional high-pressure veining close to peak-metamorphic conditions. Fluid compositions of the H_2O inclusions in kyanite would, therefore, reflect the fluid regime during the prograde and peak-metamorphic evolutionary stages. These observations, as well as the presence of H_2O-bearing minerals such as zoisite, paragonite and phengite in the veins and the eclogite, reflect elevated water fugacity in these rocks during the HP event (see also Holland 1979; Jamtveit et al. 1990; Brunsmann et al. 2000).

The initial trapping conditions of the texturally pseudosecondary CO_2 fluid inclusions (type 2) within vein quartz are difficult to assess. These fluids may have been derived from decarbonation of marbles and calc-silicate rocks present in the tectono-metamorphic units hosting the eclogites and high-pressure veins. The CO_2 phase contains no other gas species such as N_2, which are usually present within high-density CO_2-rich fluid inclusions in eclogite terranes (Klemd et al. 1992; Andersen et al. 1993; Klemd et al. 1995). The N_2 trapped in such prograde to peak-metamorphic high-density fluid inclusions can be derived from reactions involving the

Fig. 12 Position of the isochores of the different fluid inclusion types in the P–T space and schematic P–T path (*black*) of the Dabie Shan high-pressure rocks

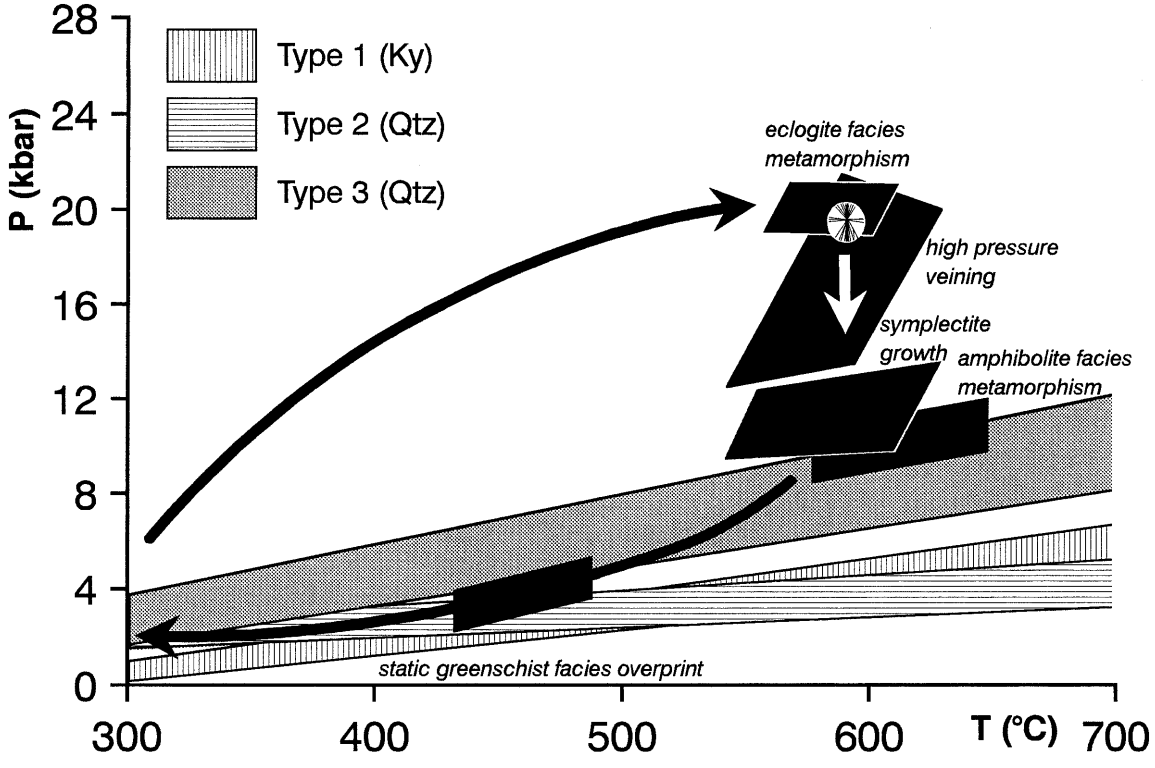

breakdown of micas and/or K-feldspar (Andersen et al. 1993). The absence of significant amounts of N_2 in the CO_2 fluid inclusions trapped in recrystallised quartz may be indicative of an effective dilution of the N_2 generated during the prograde to peak-metamorphic evolution.

The prograde dehydration reactions generated a fluid phase dominated by H_2O, as demonstrated by the fluid inclusions trapped in kyanite (type 1) close to the peak metamorphic conditions, whereas CO_2 is entirely absent within these inclusions. In contrast, no texturally primary or pseudosecondary CO_2–H_2O–NaCl or H_2O–NaCl fluid inclusions could be found in the recrystallised vein quartz. The absence of H_2O in the CO_2 fluid inclusions trapped in quartz can be explained by two entirely different processes. Either the fluid phase that was trapped in these inclusions had a very low H_2O activity or the composition of these inclusions was changed through post-entrapment modifications. It is well known that CO_2–H_2O inclusions are subjected to preferential H_2O loss during recrystallisation of the host quartz crystals, thereby producing CO_2 fluid inclusions (e.g. Hollister 1990; Bakker and Jansen 1991; Johnson and Hollister 1995). No evidence was observed to suspect fluid–fluid-immiscibility using the criteria of Ramboz et al. (1982). Alternatively, enhanced regional devolatilisation through veins and fractures during conditions of initial extension following the peak metamorphic stage could have most effectively led to the expulsion of the prograde H_2O–NaCl fluids and finally, resulted in a relative fluid deficiency. Increased decarbonation of marbles and calc-silicate rocks during the initial isothermal decompression stage of the P–T-evolution would have also generated a relatively pure CO_2 fluid phase to be trapped within the recrystallised quartz. Alternatively, such CO_2 fluids may have been supplied from an external reservoir.

The CO_2 fluids within vein quartz were most probably trapped during the isothermal decompression stage following post D1 extensional high-pressure veining and finally resulting in static symplectite growth and syntectonic (D2) amphibolite facies metamorphism. Strong recrystallisation of the vein quartz during the P–T-evolution following amphibolite facies metamorphism resulted in re-equilibration of the CO_2 fluid inclusions. The calculated densities reflect the final stage of re-equilibration during greenschist facies conditions, as densities of inclusions that were trapped or retrapped during recrystallisation of quartz will monitor those P–T conditions (e.g. Johnson and Hollister 1995).

The H_2O inclusions in kyanite as well as the CO_2 inclusions in recrystallised quartz were extensively re-equilibrated during the relatively late greenschist facies P–T-conditions (see Fig. 12). Such a process explains the variation in densities for both types of inclusions. Modified fluid inclusions of the same shape should reveal a correlation between Th and inclusion size because larger inclusions, as a result of pressure differences, re-equilibrate before smaller inclusions during exhumation (e.g. Bodnar et al. 1989; Hall et al. 1991; Klemd et al. 1995). Such a correlation, however, is not observed in the investigated samples. However, even small inclusions (< 10 μm) will re-equilibrate as a result of large pressure gradients during exhumation. Furthermore, preferential loss of H_2O during re-equilibration of the smaller inclusions as described by Hall and Sterner (1993) cannot be proven, as there is no correlation between inclusion size and salinity. The fact that some inclusions of both inclusion types seem to have decrepitated or re-equilibrated during post-amphibolite facies conditions, is probably the result of individual fluid density geometry as well as size of inclusion.

The secondary H_2O inclusions (type 3) trapped along healed fracture zones in vein quartz can be related to the latest evolutionary stage of the high-pressure veins. Fracturing and infiltration by these low-salinity H_2O fluids took place under dominantly brittle conditions subsequent to the latest recrystallisation of vein quartz. As minimum temperatures for the recrystallisation of quartz are usually assumed to be in the range of 270–300 °C (Voll 1969), this fluid phase clearly penetrated the rock at the last stage of orogenic evolution.

U–Pb systematics of rutile

The three analysed samples of specimen HVP1 are small fragments from a 4-cm-long single rutile crystal. They are characterised by little radiogenic lead, and very low uranium contents (< 0.1 ppm; Table 6). The isotopic variability among them is, however, too large to be attributed to in-situ lead growth (Fig. 13) and patterns on the $^{206}Pb/^{204}Pb$-$^{207}Pb/^{204}Pb$ and $^{206}Pb/^{204}Pb$–$^{208}Pb/^{204}Pb$ are incompatible with secondary addition or removal of lead. Note that, although blank lead (15 ± 8 pg) contributes significantly to total lead in samples 1–3 (170–180 pg), the observed variation in the isotopic composition is not compatible with incorrect estimation of blank level or composition. Thus, the initial lead composition of rutile from specimen HVP1 was isotopically heterogeneous, which implies that the lead in the fluid was isotopically variable during rutile crystallisation. This heterogeneity may reflect a genuine character of the inflowing fluid or may reflect local wallrock–fluid interaction, notably leaching or dissolution of the wallrock (e.g. Banks et al. 1991; Romer and Heinrich 1998). The low uranium contents in this specimen reflect low availability of uranium in the fluid or the preferential partitioning of uranium into the fluid.

Rutile in specimen HPV2b occurs in a medium-grained zone in the vein. Three analysed samples show variably radiogenic lead. Two samples have uranium contents at ~3 ppm and low lead contents. Their lead isotopic composition is distinctly radiogenic. The third sample has little uranium and a high content of lead. Its lead isotopic composition, thus, still closely resembles the initial composition acquired at the time of rutile crystallisation. Using this isotopic composition initially for the other two analysed samples results in $^{206}Pb/^{238}U$

Table 6 Pb–Pb and U–Pb analytical data of rutile from high-pressure veins

Sample[a]	Weight (mg)	Concentrations (ppm) U	Pbtot	$^{206}Pb/^{204}Pb$ Measured ratios[b]	$^{206}Pb/^{204}Pb$ corr.[c]	$^{207}Pb/^{204}Pb$ corr.[c]	$^{208}Pb/^{204}Pb$ corr.[c]	$^{238}U/^{204}Pb$ corr.[d]
Rutile								
Sample HPV1								
1	0.319	≪0.1	1.11	18.121	17.87	15.37	37.18	–
2	0.347	< 0.07	0.46	19.086	18.70	15.66	38.67	–
3	0.638	< 0.08	0.23	19.541	19.05	15.33	37.63	–
Sample HPV2b								
4[e,f]	0.587	3.19	0.24	57.248	6329	17.60	37∼52	1,360
5[e,f]	0.509	3.28	0.35	43.615	46.09	16.85	38.41	820
6	0.749	< 0.16	6.38	19.409	19.43	15.69	38.60	–

[a] Rutile concentrates were obtained using standard mineral-separation procedures and were purified through separation by hand under the binocular. Care was taken to use only fracture-free and inclusion free clear crystals or crystal fragments. ^{205}Pb–^{235}U mixed tracer was added before sample dissolution. All samples were dissolved with 52% Hf in autoclaves at 220 °C for 4 days, dried, and transferred overnight into chloride-form using 6 N HCl. Lead and uranium were separated using ion-exchange chromatography as described by Tilton (1973) and Manhés et al. (1978). Lead and uranium were loaded on separate single Rc-filaments using silica-gel emitter and H_3PO_4 (Gerstenberger and Haase 1997) and analysed at 1,200–1,260 °C and 1,350–1,400 °C, respectively, on a Finnigan MAT262 multicollector mass-spectrometer using ion counting

[b] Lead isotope ratios corrected for fractionation with 0.1%/a.m.u.

[c] Lead corrected for fractionation, 15 pg lead blank, and tracer contribution. Because of very low total lead contents, blank and tracer lead represent significant contributions. Uncertainties of 0.3–0.4% for isotope ratios were calculated taking into consideration the following uncertainties: measurement errors, 30% for fractionation correction, 50% for blank level, 0.1, 0.05, 0.2 for $^{206}Pb/^{204}Pb$, $^{207}Pb/^{204}Pb$, and $^{208}Pb/^{204}Pb$ blank composition, respectively, and $^{205}Pb/^{206}Pb = 21.693$ for isotopic tracer composition. Data reduction was performed by Monte Carlo modelling of 1,000 random normally distributed data sets that fit above uncertainty limits, allowing for error correlation when appropriate

[d] Lead corrected for fractionation, 15 pg lead blank, tracer contribution, and initial lead. Uranium corrected for fractionation and 1 pg uranium blank

[e] The Pb/U ratios are very dependent on the common lead corection. The here calculated Pb/U and age values are for illustration of the effects of initial isotopic heterogeneity and do not necessarily represent the preferred values. For common lead $^{206}Pb/^{204}Pb = 17.5 \pm 0.1$, $^{207}Pb/^{235}Pb = 15.4 \pm 0.05$, $^{208}Pb/^{204}Pb = 37.0 \pm 0.2$ (Fig. 13), Pb/U ratios are $^{206}Pb/^{238}U = 0.0337$ and $^{207}Pb/^{235}U = 0.223$ (analysis 4) and $^{206}Pb/^{238}U = 0.0349$ and $^{207}Pb/^{235}U = 0.244$ (analysis 5). Using the constants of Jaffey et al. (1971) recommended by IUGS (Steiger and Jäger 1977), the corresponding $^{206}Pb/^{238}U$ ages are 214 Ma (analysis 4) and 221 Ma (analysis 5)

[f] As in e with common lead $^{206}Pb/^{204}Pb = 19.0 \pm 0.1$, $^{207}Pb/^{204}Pb = 15.65 \pm 0.05$, $^{208}Pb/^{204}Pb = 38.3 \pm 0.2$ (Fig. 13), the following values are obtained: analysis 4: $^{206}Pb/^{238}U = 0.0326$, $^{207}Pb/^{235}U = 0.198$ and $^{206}Pb/^{238}U_{age} = 207$ Ma; and analysis 5: $^{206}Pb/^{238}U = 0.0331$ and $^{207}Pb/^{235}U = 0.202$ and $^{206}Pb/^{238}U_{age} = 210$ Ma

and $^{207}Pb/^{235}U$ and indicates that (1) the plot to the left of the concordia, i.e. the $^{207}Pb/^{204}Pb$ used for the common lead correction was too high, and (2) that they differ slightly in their apparent $^{206}Pb/^{238}U$ age from 207–210 Ma (Table 6, see footnote). Given the initial lead isotopic heterogeneity of rutile in specimen HPV1, there is little reason to assume that the initial lead isotopic composition of rutile in specimen HVP2b would be homogeneous. Thus, the rutile data were also calculated using the least radiogenic lead isotopic composition observed in the veins. Then, the two radiogenic rutile samples yield apparent $^{206}Pb/^{238}U$ ages at 221 and 214 Ma (Table 6) respectively.

Additional arguments for a heterogeneous initial lead isotopic composition in rutile specimen HVP2b come from the $^{206}Pb/^{204}Pb$–$^{207}Pb/^{204}Pb$–$^{208}Pb/^{204}Pb$ systematics (Table 6). (1) In the $^{206}Pb/^{204}Pb$–$^{207}Pb/^{204}Pb$ diagram, the three HVP2b samples fall on a line with a $^{207}Pb/^{206}Pb$ slope at 0.0435 (Fig. 13A), which is flatter than that for 'instantaneous lead formation at present' and which would correspond to a negative age if the lead line is interpreted as secondary lead isochron. (2) In the $^{206}Pb/^{204}Pb$–$^{208}Pb/^{204}Pb$ diagram (Fig. 13B), the three HVP2b samples scatter about a line with negative slope. Because $^{206}Pb/^{204}Pb$ and $^{208}Pb/^{204}Pb$ ratios only can increase with time, such a pattern would suggest either that uranium and thorium contents in rutile anticorrelate or that the initial lead isotopic composition was heterogeneous. As rutile is not known to incorporate significant amounts of thorium (cf. Mezger et al. 1989; Brenan et al. 1994), and thorium might have been little available because of its limited mobility in aqueous fluids, a heterogeneous initial lead isotopic composition seems to be the more likely explanation. (3) The slope of the regression line in the $^{206}Pb/^{204}Pb$–$^{238}U/^{204}Pb$ diagram is too flat to be in agreement with the $^{206}Pb/^{238}U$ data (not shown).

Constraints on the age of rutile. Because of the heterogeneous nature of the initial lead isotopic composition, it is not possible to determine a precise age for rutile crystallisation. It should be noted that the range in apparent $^{206}Pb/^{238}U$ ages from 207 to 221 Ma (1) is entirely caused by the uncertainty in the true common lead composition and (2) represents a minimum range, as it is possible that the initial lead of the dated fragments has even a less radiogenic lead isotopic composition than observed for the low-U fragments (Table 6). In this case, the apparent $^{206}Pb/^{238}U$ age would be older. The dependence of the rutile age on the common lead composition is also illustrated in Fig. 13C using samples 4

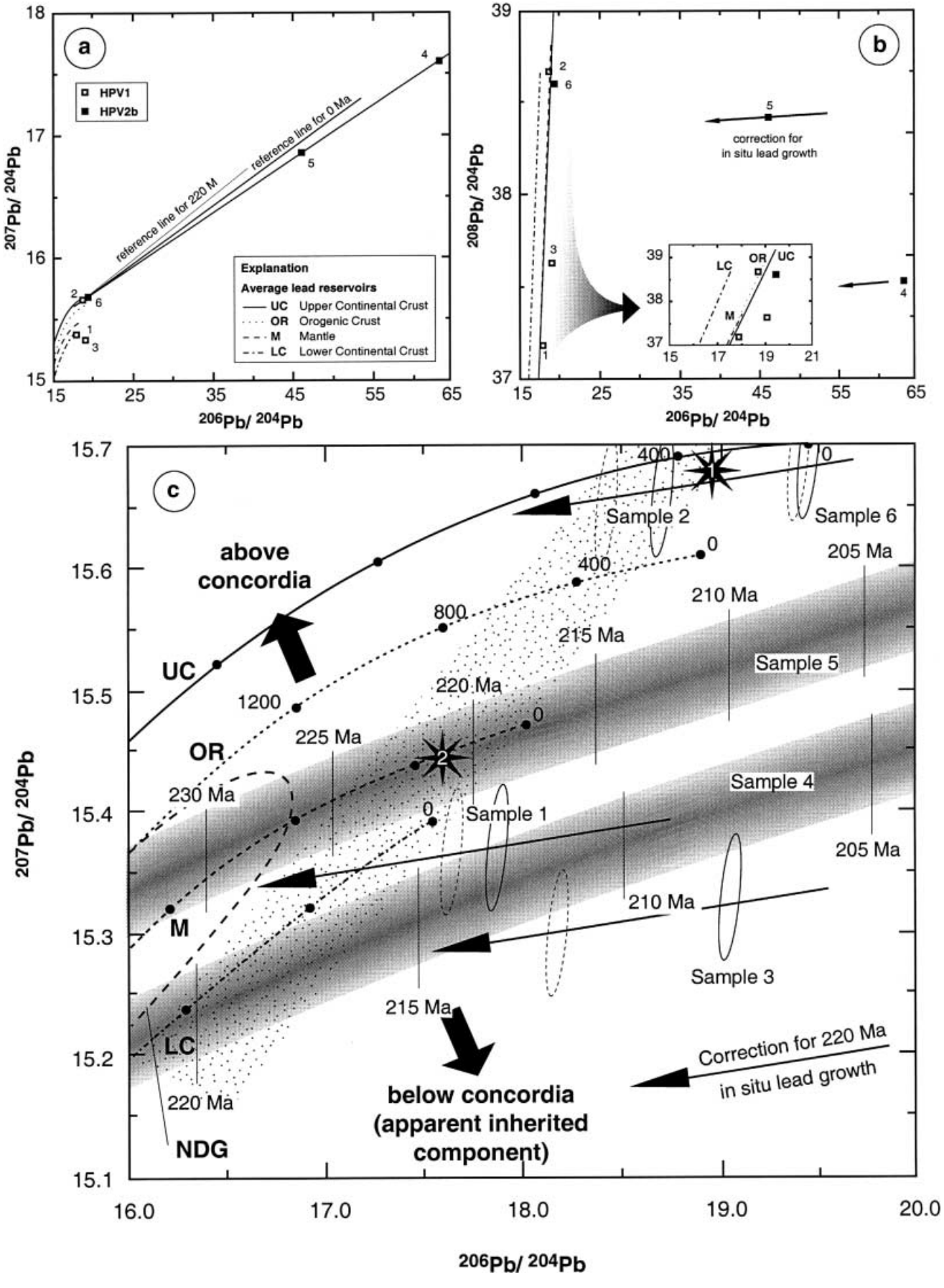
a
HPV1
HPV2b
reference line for 220 M
reference line for 0 Ma
Explanation
Average lead reservoirs
UC Upper Continental Crust
OR Orogenic Crust
M Mantle
LC Lower Continental Crust
207Pb/ 204Pb
206Pb/ 204Pb
b
correction for
in situ lead growth
208Pb/ 204Pb
206Pb/ 204Pb
c
above
concordia
UC
OR
M
LC
NDG
Sample 1
Sample 2
Sample 3
Sample 4
Sample 5
Sample 6
205 Ma
210 Ma
215 Ma
220 Ma
225 Ma
230 Ma
below concordia
(apparent inherited
component)
Correction for 220 Ma
in situ lead growth
207Pb/ 204Pb
206Pb/ 204Pb

◀

Fig. 13 Pb–Pb diagrams for rutile samples from Dabie Shan high-pressure veins. Sample numbers as in Table 6. Evolution curves for average lead reservoirs (Zartman and Doe 1981) are for reference only. **A** $^{206}Pb/^{204}Pb$–$^{207}Pb/^{204}Pb$ diagram. Note excess scatter at low $^{206}Pb/^{204}Pb$ and the slope of the regression line, which is flatter than the reference lines for 0 and 220 Ma, respectively. **B** $^{206}Pb/^{204}Pb$–$^{208}Pb/^{204}Pb$ diagram. Note the large variation of $^{208}Pb/^{204}Pb$, which for a low-Th phase is not reconcilable with in-situ lead growth. **C** $^{206}Pb/^{204}Pb$–$^{207}Pb/^{204}Pb$ diagram, (*enlargement* from **A**). *Shaded arrays* for samples 4 and 5 are calculated using the measured lead isotopic composition, the Pb and U contents, and the ages indicated by the *short vertical lines* and assuming that rutile represents a closed system for U and Pb, i.e. (1) any assumption of initial lead falling on a shaded array would yield a concordant age in the concordia for that sample, and (2) the $^{206}Pb/^{238}U$ age is given by the *short vertical line*. Note that the arrays for samples 4 and 5 do not intersect each other, and thus, samples 4 and 5 cannot have had a common initial lead isotopic composition. Samples 1, 2, 3, and 6 are shown as *ellipses*; the recalculated lead isotopic composition for 220 Ma is shown as *dashed ellipses*. *Asterisks 1 and 2* refer to initial lead used to calculate data in Table 6. For lead of the lead composition shown by asterisk 1, all isotope data will fall to the left of the concordia. For lead of the lead composition shown by *asterisk 2*, sample 5 will yield concordant data and sample 4 still would plot to the left of the concordia. The lead growth curves for average lead reservoirs (Zartman and Doe 1981) are shown for orientation. The mixing array (*dotted*) is shown for illustration and does not have age significance. It is fitted (1) to encompass lead that is less radiogenic than the measured isotopic compositions and (2) to intercept the arrays of concordant data of samples 4 and 5, respectively, at the same age

and 5 from Table 6. The shaded area for each sample represents those initial lead isotopic compositions that yield concordant data in the concordia diagram, whereas the numbers refer to the age obtained. Note that concordant data are obtained for contrasting initial lead in accordance with the anomalous flat slope in the $^{206}Pb/^{204}Pb$–$^{207}Pb/^{204}Pb$ diagram (Fig. 13A) and the heterogeneous isotopic composition of the low-U rutile samples, which is given for orientation (Fig. 13C). The dotted array at ~220 Ma (Fig. 13C) is here considered to be the best estimate for the U–Pb age of the rutile crystals and the formation of these veins because this array yields a coherent age for the two fragments with radiogenic lead (samples 4 and 5) and encompasses also the least radiogenic lead observed. This estimate coincides well with the age of collision and UHP metamorphism (Ames et al. 1993, 1996; Li et al. 1993; Xiao et al. 1995; Rowley et al. 1997; Hacker et al. 1998). The lead array (dotted, Fig. 13C) by no means includes anomalously non-radiogenic lead, as shown by the range of initial lead isotopic compositions encompassed by leached K-feldspar from ~130 Ma old granitoids from the north Dabie Shan (NDG, Fig. 13C). Although the temperature of isotopic closure of rutile is debated (e.g. Mezger et al. 1989; Santos Zalduegui et al. 1996), the U–Pb systematics of rutile is here interpreted to be related with the formation of rutile rather than with some moment during the cooling history of the rock. Such an interpretation is in agreement with the recent experimental determination of lead diffusion in rutile, which corresponds to a distinctly higher temperature of isotopic closure (Cherniak 2000; ~600 °C for 100-μm large grains) and, furthermore, the large size of the analysed rutile crystal, and the preservation of the initial isotopic heterogeneity. If there had been significant mobility of Pb after crystallisation, initial isotopic heterogeneities probably would have been largely erased.

The demonstrated initial isotopic heterogeneity of lead in rutile and the general sensitivity of age determinations of minerals with low $^{206}Pb/^{204}Pb$ to the correction of initial lead have direct implications for U–Pb chronology of low-$^{206}Pb/^{204}Pb$ minerals from metamorphic rocks and fluid-dominated systems. (1) Scatter in age may not reflect secondary disturbance, slow cooling, or formation over long time. Instead, it may reflect heterogeneous initial lead isotopic compositions (for a detailed discussion see also Romer and Rötzler 2001). (2) In cases where the initial lead isotopic composition cannot be measured (phases consumed, fluid gone), the choice of initial composition will be arbitrary. Comparison of such ages with those obtained from other chronometers may result in incorrect inferences about the conditions of isotopic closure. The perfect fit of the data along a straight line (Fig. 13A) has geochronologically no significance, which is obvious from the 'future' age. Furthermore, it implies that the initial lead isotopic composition of a low-$^{238}U/^{204}Pb$ mineral not necessarily is identical with the one of cogenetic minerals with higher $^{238}U/^{204}Pb$ (and thus after some time show a more radiogenic lead isotopic compositions) and, therefore, in some cases may be unsuitable to constrain the slope of lead lines in the $^{206}Pb/^{204}Pb$-$^{207}Pb/^{204}Pb$ and $^{206}Pb/^{204}Pb$ and $^{238}U/^{204}Pb$ diagrams.

Source of Pb and fluid. The initial lead isotopic composition represents a fingerprint for the lead source, and possibly indirectly also the fluid source. The two samples with the lowest $^{207}Pb/^{204}Pb$ values (samples 1 and 3 in Table 6) also show the lowest $^{208}Pb/^{204}Pb$ values. Sample 4 (Table 6) could have the same initial lead signature, as indicated by low $^{208}Pb/^{204}Pb$ (Fig. 13B, C) and its curve of possible initial lead isotope composition, if rutile was a closed system after crystallisation. Samples 2 and 6 (Table 6) in comparison have high $^{207}Pb/^{204}Pb$ and $^{208}Pb/^{204}Pb$ values. Initial lead of sample 5 (Table 6) is intermediate between these two groups of samples in both lead diagrams (Fig. 13B, C).

Low $^{206}Pb/^{204}Pb$ ratios seem to be characteristic for the entire Dabie Shan region. For instance, leached K-feldspar from 125–140 Ma old post-metamorphic granitoid intrusions of the northern Dabie Shan range in their $^{206}Pb/^{204}Pb$ ratios from 15.8–16.7 (Romer, unpublished data). Such low $^{206}Pb/^{204}Pb$ ratios indicate that lead is derived from old rocks or minerals that are characterised by low $^{238}U/^{204}Pb$ and, therefore, had experienced only little lead growth after their formation. Low $^{238}U/^{204}Pb$ are found in rocks that had lost significant portions of uranium during high-grade metamorphism, and in feldspar-dominated magmatic and sedimentary rocks because feldspar strongly favours the

incorporation of lead over uranium. During high-grade metamorphism, not only uranium, but to a lesser extent also lead, is lost. Hence, lower-crustal rocks may have enhanced $^{232}Th/^{204}Pb$ and low $^{238}U/^{204}Pb$. These contrasting Th/Pb and U/Pb – with increasing time – result in distinct lead isotopic compositions. For instance, old lower crustal rocks are characterised by rather high $^{208}Pb/^{204}Pb$ at low $^{206}Pb/^{204}Pb$ values, whereas old feldspar-dominated rocks commonly have low $^{208}Pb/^{204}Pb$ and low $^{206}Pb/^{204}Pb$ values. The low $^{206}Pb/^{204}Pb$ for initial lead of these intrusions, as well as the initial lead of the vein-bound rutile, indicates significant amounts of concealed old basement in the Dabie Shan region.

The initial isotopic composition of rutile (projected back along lead growth-lines for 220 Ma) encompasses the entire range of isotopic composition characteristic for old lower crust, or possibly old carbonates or old feldspar-dominated rocks (Fig. 13C), and thus may originate from such sources (see reference curves in Fig. 13C). The initial lead isotopic heterogeneity of rutile demonstrates that the fluid was temporally heterogeneous in its lead isotopic composition and was derived from contrasting sources (large variation in initial $^{208}Pb/^{204}Pb$).

Fluid evolution along the P–T path

Petrographic and petrologic features suggest a subduction-related, prograde metamorphic path for the investigated rocks, passing through the stability fields of lawsonite and glaucophane (cf. Fig. 6; see also Castelli et al. 1998). Thermobarometric data demonstrate peak conditions for the HP eclogite-facies at 19–21 kbar and 570–620 °C. The HP metamorphism was accompanied by a penetrative D1 deformation, which was well preserved in the pristine eclogites. Although the exact time of formation of quartz vein HPV1 remains unclear, crosscutting relations definitely show that the formation of HPV2 post-dates the eclogite-facies D1 deformation. Mineral assemblages within quartz vein HPV2, especially the growth of garnet and omphacite, highlight its formation under eclogite facies conditions. This is also confirmed by calculations of phase equilibrium curves on the vein assemblage quartz–kyanite–talc–zoisite–garnet–aragonite using the TWEEQ-program of Berman (1991), which yield an intersection at 19.5 kbar and 591 °C in the presence of an aqueous fluid phase. These observations demonstrate that both the peak-metamorphism of the host-rocks and extensional fracturing with subsequent growth of hydrous vein-assemblages occurred under similar eclogite-facies conditions. Furthermore, it testifies that a free fluid phase may well exist in deeply subducted crust (cf. Austrheim 1998). From this the question of the source of this fluid phase arises.

Considerable amounts of fluids were released from subducted metasediments and metavolcanics (cf. Fig. 1) during the transition of blueschist-facies rocks to eclogite-facies rocks (e.g. Ridley 1984) and later during near-isothermal decompression. Another potential source of fluids is the basement of the Dabie Shan area, which also underwent dehydration in the course of the Triassic metamorphic overprint. During subsequent exhumation, fluids penetrated the rock and led to the formation of quartz veins on fractures. It is, however, unclear to what extent early produced fluids still were available during the exhumation of the HP and UHP units (gneisses and metabasites) of Dabie Shan. An indication for the origin of the fluid phase is given by the vein minerals ankerite, zoisite, paragonite and omphacite, which display similar composition to those forming their host eclogites. This correlation shows that the chemistry of the vein-filling was rock-controlled and that the fluid phase was – at least in part – locally derived (e.g. Scambelluri et al. 1998). This is also supported by the observed heterogeneous population of fluid inclusions ranging from low salinity brines to CO_2-rich inclusions. According to Giaramita and Sorensen (1994), this favours a local source for the fluid, which was generated during progressive metamorphism. Furthermore, this is in agreement with the findings of Xiao et al. (2000) who suggested that the preservation of primary high salinity inclusions in omphacite and kyanite indicate a relatively closed fluid system and a limited fluid flow during UHP-metamorphism in the Bixiling eclogites. Their model is in agreement with previous fluids inclusion studies, which indicate that large fluid activity gradients could persist during eclogite facies conditions as a consequence of local fluid production and/or buffering as well as limited fluid flow at depth >60 km in a subduction zone (e.g. Philippot and Selverstone 1991; Klemd et al. 1992).

Beside hydraulic fracturing, the formation of fractures may, however, also be induced by volume reduction during eclogitisation (Austrheim 1998) or later by hydration and volume increase during back-reaction of eclogites to amphibolites during exhumation (e.g. Heinrich 1982). The behaviour of all fluids generated during the metamorphic path of the HP and UHP rocks follows the general sequence of dehydration with build-up of an overpressure and eventual fracturing of the rocks, channelled escape of the fluids along these fractures towards lower pressure (i.e. generally lower levels). In this general sequence of processes, which occur at different depth, the fluid passes through the rocks as if they were a chromatographic column, exchanging with the rocks, and thus, changing them and becoming changed itself. Therefore, the fluid does not necessarily reflect its source, but may instead reflect the last lithological unit with which it had equilibrated. Such a local buffering of the fluid has been demonstrated for fluid inclusion isotopes from low-grade rocks in the Pyrenees (Banks et al. 1991) and for Sr and Pb isotopes from wollastonite-mantled chert layers in marbles (Romer and Heinrich 1998). The studied rocks from HPV1 and HPV2 also show this general sequence, although the various stages were recorded at different times as the samples moved through this chromatographic column. Our results concur with

those from fluid inclusion studies on UHP rocks from the Bixiling complex in Dabie Shan, by Xiao et al. (2000). These investigators showed that the fluid phase underwent distinct changes in composition during the metamorphic evolution and – to a great extent – re-equilibrated during the last stages of the metamorphism. Especially the infiltration of a low salinity aqueous phase on the retrograde metamorphic path is in concurrence with our observations from the HP rocks.

Evidence for the character of the fluid phase during the HP event is given by primary, two-phase H_2O inclusions trapped in vein kyanite. The main source for this hydrous fluid phase could be dehydration reactions that occurred in the course of the eclogite facies metamorphism in the mafic host rock and neighbouring metasediments or from destabilisation of hydrous phases during decompression. This conclusion is in accordance with the observation that eclogite-facies metamorphism is most typically accompanied by a fluid regime dominated by H_2O but, however, in places also by $N_2 \pm CO_2$ (Andersen et al. 1989; Klemd 1989; Touret 1992; Andersen et al. 1993; Klemd and Bröcker 1999). The initial lead of rutile, however, demonstrates that the mafic host rocks and the associated metasediments were not the only source of the fluid, but part of the fluid phase may have been released from old basement rocks of the Dabie Shan.

The eclogite-facies stage was followed by a static growth of symplectites, and in turn followed by a syntectonic (D2) amphibolite-facies metamorphism. In the course of this retrogression, a CO_2-rich fluid penetrated the rocks. Large amounts of the eclogite facies rocks were totally retrogressed and deformation affected even part of the high-pressure quartz veins. The last overprint took place under static greenschist facies conditions and led to a re-equilibration of all captured fluid inclusions up to this stage. Furthermore, low-salinity H_2O fluids penetrated the rocks via fracture zones. The low amount of this fluid phase and the lack of any deformation during greenschist facies metamorphism are responsible for the modest extent of this overprint.

Acknowledgements Dieter Rhede, Oona Appelt and Klaus Becker are thanked for assistance with the microprobe analyses at the GFZ Potsdam and at the University of Freiberg. Klaus-Peter Kelber at University of Würzburg kindly provided the black-and-white photographs of fluid inclusions. We are grateful to Lothar Ratschbacher and Jens C. Schmid who supplied structural data and eclogite samples from location HPV2 and we enjoyed the company and helpful comments of Dr X. Liu and Mr H. Xue during our fieldwork in China. The paper profited considerably from thorough reviews by Håkon Austrheim and Bruce Yardley. Funding was provided by the grants OB 80/17 and KL692/9 from the Deutsche Forschungsgemeinschaft (DFG).

Appendix

Compilation of the metamorphic mineral reactions for the invariant point of the high-pressure mineral assemblage in HPV2b.

1. 5 Aragonite + 3 α-quartz + 2 zoisite = 3 grossular + H_2O + 5 CO_2
2. 4 Aragonite + 3 kyanite + 3 α-quartz + H_2O = 2 zoisite + 4 CO_2
3. 9 α-Quartz + 3 pyrope + 4 aragonite + 4 H_2O = 3 talc + 2 zoisite + 4 CO_2
4. 3 Aragonite + kyanite + 2 α-quartz = grossular + 3 CO_2
5. 3 Kyanite + 3 grossular + 2 H_2O + CO_2 = aragonite + 4 zoisite
6. α-Quartz + 5 kyanite + 4 grossular + 3 H_2O = 6 zoisite
7. 8 Aragonite + pyrope + 7 α-quartz + 2 zoisite = talc + 4 grossular + 8 CO_2
8. 11 Aragonite + 3 talc + 8 zoisite = 3 pyrope + 9 grossular + 7 H_2O + 11 CO_2
9. 4 Grossular + 5 pyrope + 11 α-quartz + 8 H_2O = 6 zoisite + 5 talc
10. 3 Aragonite + pyrope + 4 α-quartz + H_2O = talc + grossular + 3 CO_2
11. Talc + α-quartz + 4 kyanite + 4 aragonite = pyrope + 2 zoisite + 4 CO_2
12. 8 Aragonite + 9 kyanite + 3 talc = 4 zoisite + 3 pyrope + H_2O + 8 CO_2
13. Pyrope + 2 α-quartz + H_2O = talc + kyanite
14. 5 Aragonite + grossular + 7 kyanite + 2 talc = 4 zoisite + 2 pyrope + 5 CO_2
15. 3 Talc + 8 kyanite + 4 grossular = 3 pyrope + 5 α-quartz + 6 zoisite
16. Talc + 11 kyanite + 8 grossular + 5 H_2O = pyrope + 12 zoisite
17. Talc + 2 kyanite + 3 aragonite = grossular + pyrope + 3 CO_2 + H_2O

These calculations were performed with the TWEEQ program of Berman (1991) using the thermodynamic dataset BA96.dat (see also Berman 1988). Aragonite data have been extracted from the VERTEX (Conolly 1990) database sup92ver.dat. The following activity models were applied: grossular, pyrope: Berman (1990); jadeite: Holland (1980, 1990); zoisite, diopside, talc, paragonite: ideal; fluid phase (estimated): water: 0.88; carbon dioxide: 0.12; kyanite, aragonite, quartz, coesite: $a = 1$.

References

Ague JJ (1997) Crustal mass transfer and index mineral growth in Barrow's garnet zone, northeast Scotland. Geology 25: 73–76

AIRGS (Anhui Institute of Regional Geological Survey) (1997) 1: 250,000 Geological map of Dabie mountains area of Anhui Province. Anhui Institute of Regional Geological Survey

Ames L, Tilton GR, Zhou G (1993) Timing of collision of the Sino-Korean and the Yangtse cratons: U–Pb zircon dating of coesite-bearing eclogites. Geology 21:339–342

Ames L, Zhou G, Xiong B (1996) Geochronology and geochemistry of ultrahigh-pressure metamorphism with implications for collision of the Sino-Korean and the Yangtze cratons, central China. Tectonics 15:472–489

Andersen T, Burke EAJ, Austrheim H (1989) Nitrogen-bearing, aqueous fluid inclusions in some eclogites from the Western Gneiss Region of the Norwegian Caledonides. Contrib Mineral Petrol 103:153–156

Andersen T, Burke EAJ, Austrheim H, Elvevold S (1993) N_2 and CO_2 in deep crustal fluids: evidence from the Caledonides of Norway. Chem Geol 103:153–165

Austrheim H (1987) Eclogitization of lower crustal granulites by fluid migration through shear zones. Earth Planet Sci Lett 81:221–232

Austrheim H (1990) The granulite–eclogite facies transition: a comparison of experimental work and a natural occurrence in the Bergen Arcs, western Norway. Lithos 25:163–169

Austrheim H (1998) Influence of fluid and deformation on metamorphism of the deep crust and consequences for the geodynamics of collision zones. In: Hacker BR, Liou JG (eds) When continents collide: geodynamics and geochemistry of ultrahigh-pressure rocks. Kluwer, Dordrecht, pp 297–323

Bakker RJ, Jansen JBH (1991) Experimental post-entrapment water loss from synthetic CO_2–H_2O inclusions in natural quartz. Geochim Cosmochim Acta 55:2215–2230

Banks DA, Davies GR, Yardley BWD, McCaig AM, Grant NT (1991) The chemistry of brines from an Alpine thrust system in the central Pyrenees; an application of fluid inclusion analysis to the study of fluid behaviour in orogenesis. Geochim Cosmochim Acta 55:1021–1030

Banno S (1959) Aegirinaugites from crystalline schists in Sikoku. J Geol Soc Jpn 65:652–657

Becker H, Jochum KP, Carlson RW (1999) Constraints from high-pressure veins in eclogites on the composition of hydrous fluids in subduction zones. Chem Geol 160:291–308

Berman RG (1988) Internally-consistent thermodynamic data for stoichiometric minerals in the system Na_2O–K_2O–CaO–MgO–FeO–Fe_2O_3–Al_2O_3–SiO_2–TiO_2–H_2O–CO_2. J Petrol 29:445–522

Berman RG (1990) Mixing properties of Ca–Mg–Fe–Mn garnets. Am Mineral 75:328–344

Berman RG (1991) Thermobarometry using multiequilibrium calculations: a new technique with petrologic applications. Can Mineral 29:833–855

Bodnar RJ, Binns PR, Hall DL (1989) Synthetic fluid inclusions. VI. Quantitative evaluation of the description behaviour of fluid inclusions in quartz at one atmosphere confining pressure. J Metamorph Geol 7:229–242

Bohlen SR, Liotta JJ (1986) A barometer for garnet amphibolites and garnet granulites. J Petrol 27:1025–1034

Brenan JM, Shaw HF, Phinney DL, Reyerson FJ (1994) Rutile-aqueous fluid partitioning of Nb, Ta, Hf, Zr, U, and Th: implications for high field strength element depletions in island-arc basalts. Earth Planet Sci Lett 128:327–339

Brey GP, Köhler T (1990) Geothermobarometry in four-phase lherzolites II. New thermobarometers, and practical assessment of existing thermobarometers. J Petrol 31:1353–1378

Brown PE (1989) FLINCOR: a microcomputer program for the reduction and investigation of fluid inclusion data. Am Mineral 74:1390–1393

Brunsmann A, Franz G, Erzinger J, Landwehr D (2000) Zoisite- and clinozoisite-segregations in metabasites (Tauern window, Austria) as evidence for high-pressure fluid–rock interaction. J Metamorph Geol 18:1–21

Carswell DA (1990) Eclogites and the eclogite facies. In: Carswell DA (ed) Eclogite facies rocks. Blackie, Glasgow, pp 1–13

Carswell DA, O'Brien PJ, Wilson RN, Zhai M (1997) Thermobarometry of phengite-bearing eclogites in the Dabie Mountains of central China. J Metamorph Geol 15:239–252

Castelli D, Rolfo F, Companioni R, Xu S (1998) Metamorphic veins with kyanite, zoisite and quartz in the Zhu–Jia–Chong eclogite, Dabie Shan, China. Island Arc 7:159–173

Cherniak DJ (2000) Pb diffusion in rutile. Contrib Mineral Petrol 139:198–207

Colomby A (1988) Métamorphisme et géochemie des roches mafiques des Alpes ouest-centrales (géoprofil Viège–Domodossola–Locarno). PhD Thesis, University Lausanne

Connolly JAD (1990) Multivariable phase diagrams: an algorithm based on generalized thermodynamics. Am J Sci 290: 666–718

Crawford ML (1981) Phase equilibria in aqueous fluid inclusions. In: Hollister LS, Crawford ML (eds) Fluid inclusions: applications to petrology, vol 6. Short course handbook. Mineral Association of Canada, Calgary, pp 75–100

Dickenson MP, Hewitt D (1986) A garnet–chlorite geothermometer. Geol Soc Am Abstr Prog 18:584

Droop GTB (1987) A general equation for estimating Fe^{3+} concentrations in ferromagnesian silicates and oxides from microprobe analyses, using stoichiometric criteria. Mineral Mag 51:431–435

Ellis DH, Green EH (1979) An experimental study of the effect of Ca upon garnet–clinopyroxene Fe–Mg exchange equilibria. Contrib Mineral Petrol 71:13–22

Etheridge MA (1983) Differential stress magnitudes during regional deformation and metamorphism: upper bound imposed by tensile fracturing. Geology 11:231–234

Gerstenberger H, Haase G (1997) A highly effective emitter substance for mass spectrometric Pb isotope ratio determinations. Chem Geol 136:309–312

Ghent ED, Stout MZ, Black PM, Brothers RN (1987) Chloritoid bearing rocks with blueschists and eclogites, northern New Caledonia. J Metamorph Geol 5:239–254

Giaramita MJ, Sorensen SS (1994) Primary fluids in low-temperature eclogites: evidence from two subduction complexes (Dominican Republic and California, USA). Contrib Mineral Petrol 117:279–292

Graham CM, Powell R (1986) A garnet–hornblende geothermometer: calibration, testing, and application to the Pelona schists, southern California. J Metamorph Geol 2:13–31

Green TH, Hellman PL (1988) Fe–Mg-partitioning between coexisting garnet and phengite at high-pressure, and comments on a garnet–phengite geothermometer. Lithos 15:253–266

Hacker BR, Wang X, Eide EA, Ratschbacher L (1996) Qinling–Dabie ultrahigh-pressure collisional orogen: a critical review of existing data and suggestions for future research. In: Yin A, Harrison TM (eds) The tectonic evolution of Asia, Rubey volume. Cambridge Univ Press, Cambridge, pp 345–370

Hacker BR, Ratschbacher L, Webb L, Ireland T, Walker D, Dong S (1998) U/Pb zircon ages constrain the architecture of the ultrahigh-pressure Qinling–Dabie Orogen, China. Earth Planet Sci Lett 161:215–230

Hacker BR, Ratschbacher L, Webb LE, McWilliams M, Ireland T, Dong S, Calvert A, Wenk HR (2000) Exhumation of the ultrahigh-pressure continental crust in east-central China: Late Triassic–Early Jurassic extension. J Geophys Res 105:13339–13364

Hall DL, Sterner SM (1993) Preferential water loss from synthetic fluid inclusions. Contrib Mineral Petrol 114:489–500

Hall DL, Bodnar RJ, Craig JR (1991) Fluid inclusion constraints on the uplift history of the metamorphosed massive sulfide deposit at Ducktown, Tennessee. J Metamorph Geol 9:551–565

Heinrich CH (1982) Kyanite–eclogite to amphibolite facies evolution of hydrous mafic and pelitic rocks, Adula nappe, central Alps. Contrib Mineral Petrol 81:30–38

Heinrich W, Althaus E (1981) Die obere Stabilitätsgrenze von Lawsonit plus Albit bzw. Jadeit. Fortschr Mineral 58:49–50

Heinrich W, Althaus E (1988) Experimental determination of the reactions 4 Lawsonite + 1 Albite = 1 Paragonite + 2 Zoisite + 2 Quartz + 6 H_2O and 4 Lawsonite + 1 Jadeite = 1 Paragonite + 2 Zoisite + 1 Quartz + 6 H_2O. N Jahrb Mineral 56:Beiheft 1, 38

Heinrich W, Gottschalk M (1995) Metamorphic reactions between fluid inclusions and mineral hosts. I. Progress of the reaction calcite + quartz = wollastonite + CO_2 in natural wollastonite-hosted fluid inclusions. Contrib Mineral Petrol 122:51–61

Hey MT (1957) A new review of the chlorites. Mineral Mag 30:245–253

Holland TJB (1979) High water activities in the generation of high-pressure kyanite eclogites of the Tauern window. Austria. J Geol 87:1–27

Holland TJB (1980) The reaction albite = jadeite + quartz determined experimentally in the range of 600–1200 °C. Am Mineral 65:129–134

Holland TJB (1990) Activities of components in omphacitic solid solution. Contrib Mineral Petrol 105:446–453

Hollister LS (1990) Enrichment of CO_2 in fluid inclusions in quartz by removal of H_2O during crystal-plastic deformation. J Struct Geol 12:895–901

Holloway JR (1981) Compositions and volumes of supercritical fluids in the Earth's crust. In: Hollister LS, Crawford ML (eds) Fluid inclusions: applications to petrology. Short course handbook, vol 6. Mineral Association of Canada, pp 13–38

Jaffey AH, Flynn KF, Glendenin LE, Bentley WC, Essling AM (1971) Precision measurement of half-lives and specific activities of ^{235}U and ^{238}U. Phys Rev C4:1889–1906

Jamtveit B, Bucher-Nurminen K, Austrheim H (1990) Fluid controlled eclogitization of granulites in deep crustal shear zones, Bergen arcs, western Norway. Contrib Mineral Petrol 104:184–193

Jarosewich E, Nelen JA, Norberg JA (1980) Reference samples for electron microprobe analysis. Geostandards Newslett 4:43–47

Johnson EL, Hollister LS (1995) Syndeformational fluid trapping in quartz: determining the pressure–temperature conditions of deformation from fluid inclusions and the formation of pure CO_2 fluid inclusions during grain boundary migration. J Metamorph Geol 13:239–249

Klemd R (1989) P–T evolution and fluid inclusion characteristics of retrograded eclogites, Münchberg Gneiss Complex, Germany. Contrib Mineral Petrol 102:221–229

Klemd R, Bröcker M (1999) Fluid influence on mineral reactions in ultrahigh-pressure granulites: a case study in the Snieznik Mts (West Sudetes, Poland). Contrib Mineral Petrol 136:358–373

Klemd R, van den Kerkhof AM, Horn EE (1992) High-density CO_2–N_2 inclusions in eclogite-facies metasediments of the Münchberg Gneiss complex, SE Germany. Contrib Mineral Petrol 111:409–441

Klemd R, Bröcker M, Schramm J (1995) Characterisation of amphibolite-facies fluids of Variscan eclogites from the Orlica–Snieznik dome (Sudetes, SW Poland). Chem Geol 119:101–113

Kohn MJ, Spear FS (1989) Empirical calibration of geobarometers for the assemblage garnet + hornblende + plagioclase + quartz. Am Mineral 74:77–84

Kohn MJ, Spear FS (1990) Two new geobarometers for garnet amphibolites, with applications to southeastern Vermont. Am Mineral 75:89–96

Kretz R (1983) Symbols for rock-forming minerals. Am Mineral 68:277–279

Krogh RE (1988) The garnet–clinopyroxene Fe–Mg geothermometer – a reinterpretation of existing experimental data. Contrib Mineral Petrol 99:44–48

Krogh RE (2000) The garnet–clinopyroxene Fe^{2+}–Mg geothermometer: an updated calibration. J Metamorph Geol 18(2):211–219

Laird J, Albee AL (1981) Pressure, temperature, and time indicators in mafic schists: their application to reconstructing the polymetamorphic history of Vermont. Am J Sci 281:127–175

Leake BW, Wooley AR, Arps CES, Birch WD, Gilbert MC, Grice JD, Hawthorne FC, Kato A, Kisch HJ, Krivovichev VG, Linthout K, Laird J, Mandarino J, Maresch WV, Nickel EH, Rock NMS, Schumacher JC, Smith DC, Stephenson NCN, Ungaretti L, Whittaker EJW, Youzhi G (1997) Nomenclature of amphiboles. Report of the subcommittee on amphiboles of the International Mineralogical Association Commission on new minerals and mineral names. Eur J Mineral 9:623–651

Li SG, Xiao YL, Liu DL, Chen YZ, Ge N, Zhang Z, Sun SS, Cong B, Zhang R, Hart SR, Wang S (1993) Collision of the North China and Yangtse blocks and formation of coesite-bearing eclogites; timing and processes. Chem Geol 109:89–111

Liou JG, Wang Q, Zhang RY, Zhai M, Cong BL (1995) Ultrahigh-P metamorphic rocks and their associated lithologies from the Dabie Mountains, central China: a field trip guide to the 3rd international eclogite field symposium. Chin Sci Bull Suppl 40:1–66

Liou JG, Zhang RY, Eide EA, Maruyama S, Wang X, Ernst WG (1996) Metamorphism and tectonics of high-P and ultrahigh-P belts in Dabie–Sulu regions, eastern central China. In: Yin A, Harrison TM (eds) The tectonic evolution of Asia, Rubey volume IX. Cambridge University Press, Cambridge, pp 300–343

Manhès G, Minster JF, Allègre CJ (1978) Comparative uranium–thorium–lead and rubidium–strontium study of the Saint Séverin amphoterite: consequences for early solar system chronology. Earth Planet Sci Lett 39:14–24

Manning CE (1994) Fractal clustering of metamorphic veins. Geology 22:335–338

Maresch W (1977) Experimental studies on glaucophane: an analysis of present knowledge. Tectonophysics 43:109–125

Massonne H-J (1991) High pressure low temperature metamorphism of pelites and other protoliths based on experiments in the system K_2O–MgO–Al_2O_3–SiO_2–H_2O. Habil Thesis, Univ Bochum

Mattauer M, Matte P, Malavieille J, Tapponnier P, Maluski H, Qin X, Lun L, Qin T (1985) Tectonics of the Qinling belt: build up and evolution of eastern Asia. Nature 317:496–500

Mezger H, Hanson GN, Bohlen SR (1989) High-precision U–Pb ages of metamorphic rutile: application to the cooling history of high-grade terranes. Earth Planet Sci Lett 96:106–118

Newton RC, Haselton HT (1981) Thermodynamics of the garnet–plagioclase–Al_2SiO_5–quartz geobarometer. In: Newton RC, Navrotzky A, Wood BJ (eds) Thermodynamics of minerals and melts. Springer, Berlin Heidelberg New York, pp 129–145

Okay AI (1993) Petrology of a diamond and coesite bearing metamorphic terrain: Dabie Shan, China. Eur J Mineral 5:659–667

Papike JJ, Ross M, Baldwin K (1974) Amphiboles and pyroxenes: characterization of other than quadrilateral components and estimates of ferric iron from microprobe data. Geol Soc Am Abstr Prog 6:1053–1054

Passchier CW, Trouw RAJ (1996) Microtectonics. Springer, Berlin Heidelberg New York

Philippot P, Selverstone J (1991) Trace-element-rich brines in eclogitic veins; implications for fluid composition and transport during subduction. Contrib Mineral Petrol 106:417–430

Ramboz C, Pichavaut M, Weisbrod A (1982) Fluid immiscibility in natural processes: use and misuse of fluid inclusion data. II. Interpretation of fluid inclusion data in terms of immiscibility. Chem Geol 37:29–48

Ramsay JG, Huber MI (1983) The techniques of modern structural geology, vol 1. Strain analysis. Academic Press, London

Ratschbacher L, Hacker BR, Calvert A, Webb LE, Ireland T, McWilliams M, Dong S (2000) Exhumation of the ultrahigh-pressure continental crust in east-central China: Cretaceous and Cenozoic unroofing and the Tan–Lu Fault. J Geophys Res 105:13303–13338

Ridley J (1984) Evidence of a temperature-dependent blueschist to eclogite transformation in high pressure metamorphism of metabasic rocks. J Petrol 25:852–870

Roedder E (1984) Fluid inclusions. Reviews in mineralogy, vol 12. Mineral Soc Am

Romer RL, Heinrich W (1998) Transport of Pb and Sr in leaky aquifers of the Bufa Del Diente contact metamorphic aureole, north-east Mexico. Contrib Mineral Petrol 131:155–170

Romer RL, Rötzler J (2001) P–T–t evolution of ultrahigh-temperature granulites from the Saxon Granulite Massif, Germany. Part II. Geochronology. J Petrol (in press)

Rowley DB, Xue F, Tucker RD, Peng ZX, Baker J, Davis A (1997) Ages of ultrahigh pressure metamorphism and protolith orthogneisses from the eastern Dabie Shan: U/Pb zircon geochronology. Earth Planet Sci Lett 151:191–203

Santos Zalduegui JF, Schärer U, Ibarguchi JIG, Girardeau J (1996) Origin and evolution of the Paleozoic Cabo Ortegal ultramafic–mafic complex (NW Spain): U–Pb, Rb–Sr and Pb–Pb isotope data. Chem Geol 129:281–304

Scambelluri M, Pennachioni G, Phillipot P (1998) Salt-rich aqueous fluids formed during eclogitization of metabasites in the Alpine continental crust (Austroalpine Mt. Emilius unit, Italian Western Alps). Lithos 43:151–167

Schliestedt M (1980) Phasengleichgewichte in Hochdruckgesteinen von Sifnos, Griechenland. PhD Thesis, TU Braunschweig

Schmid R, Franz L, Oberhänsli R, Dong S (2000) High Si-phengite, mineral chemistry and P–T evolution of ultra-high-pressure eclogites and calc-silicates from the Dabie Shan, eastern PR China. Geol J vol 35:185–207

Spear FS (1980) The NaSi = CaAl exchange equilibria between plagioclase and amphibole. Contrib Mineral Petrol 72:33–41

Spear FS (1991) On the interpretation of peak metamorphic temperatures in the light of garnet diffusion during cooling. J Metamorph Geol 9:379–388

Steiger RH, Jäger E (1977) Subcommission on geochronology: convention on the use of decay constants in geo- and cosmochronology. Earth Planet Sci Lett 36:359–362

Tilton GR (1973) Isotopic lead ages of chondritic meteorites. Earth Planet Sci Lett 19:321–329

Touret JLR (1992) Fluid inclusions in subducted rocks. Proc K Ned Akad Wet 95:385–403

Voll G (1960) New work on petrofabrics. Geol J 213:503–567

Voll G (1969) Klastische Minerale aus den Sedimentserien der Schottischen Highlands und ihr Schicksal bei aufsteigender Regional- und Kontaktmetamorphose. Habil Thesis, TU Berlin

von Raumer JF (1984) The External Massifs, relics of the Variscan Basement in the Alps. Geol Rundsch 73:1–31

Wang X, Jing Y, Liou JG, Pan G, Liang W, Xia M, Maruyama S (1990) Field occurrences and petrology of eclogites from the Dabie Mountains, Anhui, central China. Lithos 25:119–131

Wang X, Liou JG, Maruyama S (1992) Coesite-bearing eclogites from the Dabie Mountains, central China: petrogenesis, P–T paths, and implications for regional tectonics. J Geol 100:231–250

Wang X, Zhang R, Liou JG (1995) UHPM terrane in east central China. In: Coleman RG, Wang X (eds) Ultrahigh pressure metamorphism. Cambridge University Press, Cambridge, pp 356–390

Waters DJ, Martin HN (1993) Geobarometry in phengite-bearing eclogites. Terra Abstr 5:410–411; updated calibration of 1996 at: http://www.earth.ox.ac.uk/~davewa/ecbar.html

Xiao YL, Li SG, Jagoutz E, Cheng W (1995) P–T–t path for coesite-bearing peridotite–eclogite association in the Bixiling, Dabie Mountains. Chin Sci Bull 40:156–158

Xiao YL, Hoefs J, van den Kerkhof AM, Fiebig J, Zheng Y (2000) Fluid history of UHP metamorphism in Dabie Shan, China: a fluid inclusion and oxygen isotope study on the coesite-bearing eclogite from Bixiling. Contrib Mineral Petrol 139:1–16

Yardley BWD (1977) An empirical study of diffusion in garnet. Am Mineral 62:793–800

Yardley BWD (1983) Quartz veins and devolatilisation during metamorphism. J Geol Soc Lond 140:657–663

Yardley BWD (1986) Fluid migration and veining in the Connemara Schists, Ireland. In: Walther JV, Wood BJ (eds) Advances in physical geochemistry, vol 5. Springer, Berlin Heidelberg New York, pp 109–131

You Z, Han Y, Yang W, Zhang Z, Wie B, Liu R (1996) The high-pressure and ultra-high-pressure metamorphic belt in the East Qinling and Dabie Mountains, China. China University of Geoscience Press, Wuhan

Zartman RE, Doe BR (1981) Pumbotectonics – the model. Tectonophysics 75:135–162

Zhang Y, Frantz JD (1987) Determination of the homogenization temperatures and densities of supercritical fluids in the system NaCl–KCl–$CaCl_2$–H_2O using synthetic fluid inclusions. Chem Geol 64:335–350